

VARIABLE EXTENDED DEPTH OF FIELD IMAGING USING FREEFORM OPTICS

by

Sara Moein

A dissertation submitted to the faculty of  
The University of North Carolina at Charlotte  
in partial fulfillment of the requirements  
for the degree of Doctor of Philosophy in  
Optical Science and Engineering

Charlotte

2022

Approved by:

---

Dr. Thomas Suleski

---

Dr. Glenn Boreman

---

Dr. Gregory Gbur

---

Dr. Matthew Davies

©2022  
Sara Moein  
ALL RIGHTS RESERVED

## ABSTRACT

SARA MOEIN. Variable extended depth of field imaging using freeform optics. (Under the direction of DR. THOMAS J. SULESKI)

Recent advancements in design, manufacturing, and metrology have enabled broader use of freeform components for high-performing optical systems. Freeform optics, which lack rotational symmetry, provide additional design freedoms that can enable compact systems with enhanced functionality. As one example, freeform optics have the potential to reduce the cost and number of required parts for Extended Depth of Field (EDoF) imaging through Point Spread Function (PSF) engineering. Imaging systems with high Numerical Aperture (NA) have shallow depth of field, meaning they create clear images only along a small longitudinal distance. Prior work has demonstrated the use of freeform components for extended depth of field imaging, but each optical system typically requires a custom phase plate. As a result, methods that can enable variable EDoF for multiple imaging systems are of particular interest.

The primary goals of this dissertation are to explore and characterize methods that leverage pairs of freeform phase plates for variable EDoF imaging. Results are addressed through three articles. The first article addresses the design and simulation of a pair of 4<sup>th</sup> order polynomial freeform surfaces to enable variable EDoF for commercial lenses with a range of NA values. The second article presents an alternate design method and enhanced performance results for a pair of logarithmic freeform surfaces for the same commercial lenses. The third article presents the fabrication and experimental performance characterization of the 4<sup>th</sup> order freeform phase plate pair. These three articles showcase the advantages freeform optics can offer in PSF engineering for EDoF imaging and methods used to design, manufacture, and characterize their performance.

## DEDICATION

To my mother and my husband, for believing in me, and for their unconditional love and unwavering support. She taught me how to dream, and he stood by me as I built my dream and for that, I am forever grateful to them.

## ACKNOWLEDGEMENTS

I would like to express my gratitude to my advisor, Prof. Thomas Suleski, for his continuous guidance and support through the course of my research. His enthusiasm for problem-solving and teaching helped me in achieving academic success. I would also like to convey my gratefulness to Prof. Glenn Boreman for his contributions to this project. His instruction and assistance have had a significant impact on my studies. I am also thankful to Dr. Matthew Davies for his guidance and our useful discussions.

I like to extend my thanks to Dr. Dustin Gurganus for precision manufacturing the optical components used in this research and to Mike Dhooghe, the research operations manager at UNC Charlotte, for his invaluable assistance and guidance during the optical component's experimental characterization. I would also like to thank Dr. Shohreh Shadalou, for developing a numerical design method that was used for part of this dissertation, and Prof. Jannick Rolland (Univ. of Rochester), Dr. Christoph Menke (Carl Zeiss AG), and Dr. Sébastien Héron (THALES) for their valuable input and encouragement.

Last but not least, I would like to thank my lab mates and colleagues who have contributed to my academic endeavors in many ways: Dr. Jason Shultz, Steven Glass, Dr. Jonathon Koerber, Dr. Shohreh Shadalou, and Luke DeMars.

This work was funded through the Center for Freeform Optics and a UNC Charlotte GASP/Fellowship.

## TABLE OF CONTENTS

LIST OF TABLES.....	ix
LIST OF FIGURES.....	x
LIST OF ABBREVIATIONS.....	xiv
 CHAPTER 1: INTRODUCTION	
1.1 Background and Motivation: Extended Depth of Field Imaging .....	1
1.2 Background and Motivation: Freeform optics .....	3
1.3 Freeform Optical Systems for Variable EDoF Imaging .....	5
1.4 Dissertation outline .....	5
 CHAPTER 2: FREEFORM OPTICS FOR VARIABLE EXTENDED DEPTH OF FIELD IMAGING	
2.1 Abstract.....	8
2.2 Introduction.....	8
2.3 Design approach.....	13
2.3.1 Variable phase plate design	
2.3.2 optical design and optimization	
2.4 Design results.....	17
2.4.1 Cubic Phase Plate (CPP) design	
2.4.2 Quartic Phase Plate Pair (QPPP) design	
2.5 Performance comparisons.....	18
2.5.1 On-axis performance	
2.5.1.1 Through-focus spot diagram	
2.5.1.2 Through-focus MTF	

2.5.1.3 Root-Mean-Square (RMS) deviation and slope of RMS deviation of PSF	
2.5.2 Off-axis system performance	
2.5.2.1 Through-focus spot diagram vs. field angle	
2.5.2.2 MTF vs. field angle	
2.6 Discussion and conclusion.....	27
2.7 References.....	28
 CHAPTER 3: PSF ENGINEERING WITH VARIABLE LOGARITHMIC PHASE PLATES FOR EXTENDED DEPTH OF FIELD	
3.1 Abstract.....	32
3.2 Introduction.....	32
3.3 Design approach and results .....	35
3.3.1 Logarithmic phase plate design and optimization	
3.3.2 Variable logarithmic phase plate design and optimization	
3.4 LPP and VLPPP performance analysis .....	40
3.4.1 On-axis system performance	
3.4.1.1 Through-focus spot diagram	
3.4.1.2 Through-focus MTF	
3.4.1.3 Root-Mean-Square (RMS) deviation and slope of RMS deviation of PSF	
3.4.2 Off-axis system performance	
3.4.2.1 Through-focus spot diagram vs. field angle	
3.4.2.1 MTF vs. field angle	

3.5 LPP and VLPPP performance comparison to CPP and QPPP.....	47
3.6 Discussion and conclusion.....	49
3.7 References.....	52
<b>CHAPTER 4: FABRICATION AND CHARACTERIZATION OF FREEFORM OPTICS FOR VARIABLE EXTENDED DEPTH OF FIELD IMAGING</b>	
4.1 Abstract.....	57
4.2 Introduction.....	57
4.3 Optical and Optomechanical Fabrication .....	60
4.3.1 Optical system architecture	
4.3.2 Manufacturing of optomechanical fixturing	
4.3.2 Optical fabrication	
4.4 Performance Characterization Method, Results and Analysis .....	66
4.4.1 Autostigmatic and point source microscopes	
4.4.2 Use of PSM to characterize through-focus performance	
4.4.3 Performance characterization	
4.4.3.1 Through-focus spot measurements	
4.4.3.2 Root-Mean-Square (RMS) deviation of spots	
4.5 Discussion and Conclusion.....	74
4.6 References.....	75
<b>CHAPTER 5: CONCLUSION</b>	
5.1 Summary of work.....	81
5.2 Future work.....	82
<b>REFERENCES.....</b>	<b>84</b>

## LIST OF TABLES

Table 2-1: Optimization frequencies used to design EDoF phase plates for the selected aspheric lenses .....	16
Table 2-2: Cubic phase plate optimization results .....	18
Table 2-3: Quartic phase plate pair design results .....	18
Table 3-1: Optimization frequencies used to design EDoF phase plates for the selected aspheric lenses .....	37
Table 3-2: The LPP surface coefficients and sags for lenses with 0.25, 0.33 and 0.50 NA values .....	37
Table 3-3: VLPPP design results .....	39
Table 4-1: Cubic phase plate optimization results .....	59
Table 4-2: Quartic phase plate pair design results .....	59

## LIST OF FIGURES

Figure 1-1: Depth of field variation with lens NA.....	1
Figure 1-2: Schematic of an extended depth of field imaging system with pupil mask, using the “demo picture” provided for image simulation by Zemax OpticStudio™ .....	2
Figure 1-3: Variable power lenses using a pair of shifted freeform surfaces .....	4
Figure 2-1: Schematic of immediate (blurry) and final (in-focus) images (using the “demo picture” provided for the image simulation in Zemax OpticStudio™), created by an imaging system with EDoF phase plate.....	10
Figure 2-2: Through-focus spot diagrams for 0.33 NA aspheric lens: (a) without and (b) with a cubic phase plate. The diffraction-limited spot size and location is indicated by the black spot in each diagram.....	11
Figure 2-3: Representative images of the EDoF systems considered in this manuscript. Two fixed Phase Plates (PP1 and PP2) may be replaced with one pair of freeform phase plates to enable EDoF through the relative translation of the phase plates along the x-axis .....	13
Figure 2-4: Schematic of a pair of plano-freeform components (a) with no lateral shift and (b) with shifts along the x-axis of equal amount and opposite direction .....	14
Figure 2-5: (a) Surface of designed CPP for 0.33 NA lens and (b) surface of one of the quartic phase plates .....	17
Figure 2-6: Through-focus spot diagrams for the three aspheric lenses with fixed CPP's and variable QPPP .....	19
Figure 2-7: Tangential MTF at the best focus for the (a) 0.25, (b) 0.33, and (c) 0.50 NA lenses with and without EDoF phase plates.....	19
Figure 2-8: On-axis through-focus tangential MTF plots for the (a) 0.25, (b) 0.33, and (c) 0.50 NA lenses with and without EDoF phase plates at $f = 80$ cycles/mm .....	20
Figure 2-9: Normalized PSF for the 0.33 NA lens with CPP at best focus and $\pm 4\Delta z$ .....	21

Figure 2-10: RMS deviation of PSF through focus for the (a) 0.25, (b) 0.33, and (c) 0.50 NA lenses with and without EDoF phase plates .....	22
Figure 2-11: Slope of RMS deviation of PSF through focus for the (a) 0.25, (b) 0.33, and (c) 0.50 NA lenses with and without EDoF phase plates .....	23
Figure 2-12: Through-focus spot diagrams for 0.33 NA lens with CPP and QPPP over 3-degree field angle range along the y-axis .....	24
Figure 2-13: Best focus tangential MTF plots at 0,1 and 3-degree field angles along the y-axis for (a) 0.33 NA aspheric lens, and 0.33 NA lens with (b) CPP and (c) QPPP .....	25
Figure 2-14: Best focus tangential MTF plots at 1-degree field angles at different orientations around the optical axis for (a) 0.33 NA aspheric lens, and the same lens with (b) CPP and (c) QPPP .....	25
Figure 2-15: Through-focus tangential modulation plots for 0.33 NA aspheric lens with and without EDoF phase plates at (a) 0, (b) 1, and (c) 3-degree field angle at $f = 61$ cycles/mm .....	27
Figure 3-1: Schematic of a 0.25 NA aspheric lens with (a) LPP and (b) VLPPP .....	34
Figure 3-2: Summary of the LPP and VLPPP design process.....	35
Figure 3-3: 3D surface map for the LPPs designed for (a) 0.25 and (b) 0.50 NA lenses over 22 mm clear aperture .....	38
Figure 3-4: 3D surface map of one of the variable logarithmic phase plates over 22 mm clear aperture.....	39
Figure 3-5: Through-focus spot diagrams for 0.25, 0.33, and 0.50 NA lenses with LPP and VLPPP.....	40
Figure 3-6: Tangential MTF at the best focus for the (a) 0.25, (b) 0.33, and (c) 0.50 NA lenses with and without EDoF phase plates.....	41
Figure 3-7: On-axis through-focus tangential MTF plots (at $f = 80$ cycles/mm) for the (a) 0.25, (b) 0.33, and (c) 0.50 NA lenses with and without LPPs and VLPPP.....	41

Figure 3-8: Normalized PSFs for the 0.33 NA lens with its respective shifted VLPPP at best focus and $\pm 4\Delta z$ image plane locations .....	43
Figure 3-9: RMS deviation of PSF through-focus and its slope for (a,d) 0.25, (b,e) 0.33, and (c,f) 0.50 NA lenses with and without the LPP and VLPPP phase plates .....	44
Figure 3-10: Location of field angles along the y-axis .....	44
Figure 3-11: Through focus spot diagrams (from $-6\Delta z$ to $+6\Delta z$ ) for the 0.33 NA lens with LPP and VLPPP over a 3-degree field angle along the y-axis .....	45
Figure 3-12: MTF at best focus for (a) 0.33 NA lens, (b) 0.33 NA lens with LPP and (c) 0.33 NA lens with VLPPP over a 3-degree field angle along the y-axis.....	46
Figure 3-13: Through-focus tangential modulation at $f = 80$ cycles/mm for 0.33 NA lens with and without EDoF phase plates at (a) (0,0), (b) (0,1), and (c) (0,3) field angles along the y-axis.....	46
Figure 3-14: Through-focus ( $-10\Delta z$ to $+10\Delta z$ ) spot diagrams for the 0.33 NA lens with and without the EDoF phase plates .....	47
Figure 3-15: Comparison of RMS deviation of PSF and its slope between previously designed CPP and QPPP with current LPP and VLPPP designs for (a,b) 0.25, (c,d) 0.33, and (e,f) 0.50 NA lenses .....	49
Figure 4-1: Two fixed Phase Plates (PP1 and PP2) are replaced with one freeform phase plate pair to enable EDoF through the relative translation of the phase plates along the x-axis [21] .....	59
Figure 4-2: Simplified image of (a) freeform surface and (b) the QPPP surface, shifted in the x-direction by distance $d$ .....	61
Figure 4-3: Exploded view of CAD model for quartic phase plate test system .....	61
Figure 4-4: A HAAS CNC Toolroom Mill with manufactured mountings.....	62
Figure 4-5: Moore Nanotech 350FG 5-axis ultraprecision diamond machining system at UNC Charlotte .....	64

Figure 4-6: Schematic of the phase plates with the machined raised outer ring.....	65
Figure 4-7: (a) Image of a finished QPP, and interferometric measurement of a finished QPPP using the Zygo Zegage™ Plus 3D optical surface profiler and the average surface roughness measurements for the (b) 20x and (c) 50x objectives.....	66
Figure 4-8: Simple Autostigmatic Microscope configuration .....	67
Figure 4-9: Measuring radius of curvature of spherical reflective surface using ASM.....	67
Figure 4-10: Schematic of a PSM, with illumination and imaging paths [1] .....	68
Figure 4-11: (a) Schematic of setup (top view) for characterization of variable EDoF imaging, and (b) experimental setup (side view) for phase plate characterization.....	69
Figure 4-12: Through-focus spot measurements from $-36\ \mu\text{m}$ to $+36\ \mu\text{m}$ ( $-6\Delta z$ to $+6\Delta z$ ), for the 0.33 NA lens with and without EDoF phase plates.....	70
Figure 4-13: Experimental RMS deviation of normalized spots from $-36\ \mu\text{m}$ to $+36\ \mu\text{m}$ ( $-6\Delta z$ to $+6\Delta z$ ), for the 0.33 NA lens with and without EDoF phase plates .....	72
Figure 4-14: Simulated PSF at best focus and measured spot at optimum focus for the 0.33 NA lens with and without EDoF phase plates .....	73
Figure 4-15: Comparison between the RMS deviation of normalized PSF (simulation) and spots (experimental) from $-36\ \mu\text{m}$ to $+36\ \mu\text{m}$ ( $-6\Delta z$ to $+6\Delta z$ ), for (a) 0.33 NA lens, (b) 0.33 NA lens with CPP and (c) 0.33 NA lens with QPPP .....	74

## LIST OF ABBREVIATIONS

CPP	Cubic Phase Plate
DoF	Depth of Field
EDoF	Extended Depth of Field
LPP	Logarithmic Phase Plate
MSE	Mean-Squared Error
MTF	Modulation Transfer Function
NA	Numerical Aperture
PSF	Point Spread Function
PSM	Point Source Microscope
QPPP	Quartic Phase Plate Pair
RMS	Root-Mean-Square
VLPPP	Variable Logarithmic Phase Plate Pair

## CHAPTER 1: INTRODUCTION

### 1.1 Background and Motivation: Extended Depth of Field Imaging

In imaging systems, the lateral resolution (Rayleigh criterion), which defines the minimum distance at which the optical system can resolve images of two point sources in the far field is inversely proportional to system Numerical Aperture (NA) [2, 3]:

$$\Delta d = \frac{0.61\lambda}{NA} . \quad (1.1)$$

In this equation,  $\lambda$  is the source wavelength and NA is system's numerical aperture, which defines how much light the imaging system accepts. Therefore, systems with larger NA values have better lateral resolution. However, Depth of Field (DoF), which is defined as the axial distance in object space over which the imaging system can form an in-focus image, is inversely proportional to NA. This behavior is illustrated in Figure 1-1 and defined as [2, 3]:

$$DoF = \frac{2n\lambda}{NA^2} , \quad (1.2)$$

where  $n$  is the refractive index of the surrounding medium, and  $\lambda$  is the source wavelength.

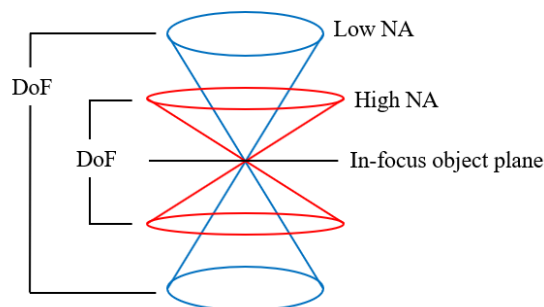


Figure 1-1: Depth of field variation with lens NA.

As a result, while systems with a higher NA have higher lateral resolution, the narrower depth of field makes image formation more difficult, particularly in applications such as microscopy at high magnification and NA.

Researchers have pioneered a variety of techniques for enabling Extended DoF (EDoF) imaging. Scanning confocal microscopy [4-7] benefits from the acquisition of multiple images via axial movement of the focused light at the sample location, and use of adaptive optics such as deformable mirrors and tunable lenses [8-12] tune the optical power for higher quality image acquisition. These two methods enable EDoF without changing the system NA or lowering the lateral resolution.

Another technique for enabling EDoF is wavefront coding [13-16]. This approach uses pupil engineering (to reduce system sensitivity to defocus) and digital image processing in order to retrieve a high-quality image [17-20]. In wavefront coding, the imaging system's Point Spread Function (PSF) is engineered to be focus-invariant over an axial range greater than the depth of field (DoF) by incorporating a mask at the exit pupil of the imaging system. This results in a blurry intermediate image, which can then be deblurred using deconvolution methods, as illustrated in Figure 1-2.

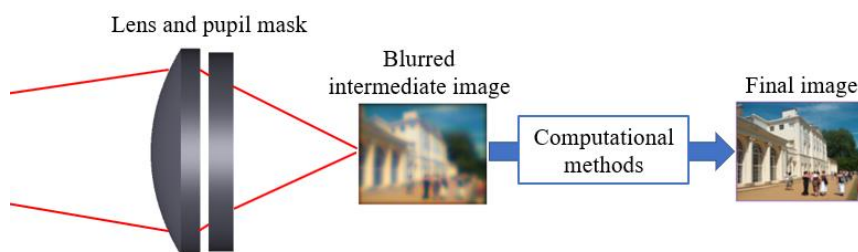


Figure 1-2: Schematic of an extended depth of field imaging system with pupil mask, using the “demo picture” provided for image simulation by Zemax OpticStudio™.

Binary annular pupil masks [21], shaded annular apodizers [22], annular apodizers based on the Bessel function [23], and absorbing apertures are all examples of amplitude EDoF masks [24, 25]. As previously stated, EDoF can also be achieved by engineering the pupil phase of the imaging system by incorporating phase plates at the exit pupil. There are two types of EDoF phase plates: rotationally symmetric and asymmetric (freeform). Logarithmic aspheres [26, 27], axicons [28-31], and binary and annular phase modulated plates [32-37] are examples for rotationally symmetric phase plates; cubic and generalized cubic [14, 38-48], logarithmic and improved logarithmic plates are prime examples for the asymmetric phase plates [49-52].

While the design and implementation of EDoF masks has demonstrated great promise for generating focus-invariant optical responses, these masks are extremely sensitive to system parameters, necessitating design of a custom mask for each system.

## 1.2 Background and Motivation: Freeform optics

By definition, surfaces with no axis of rotational symmetry are considered freeforms [53]. These surfaces can be described using different mathematical descriptions, such as Zernike, Q-type, and XY polynomials [54]. The additional degrees of freedom available in the design of freeform optical surfaces enable higher performance with fewer elements and a smaller system volume. Additionally, recent advancements in optical manufacturing and metrology have brought freeform surfaces to the forefront of attention [55].

Freeform optical components can be broadly classified into two types: static and dynamic. Static freeform optics are made up of one or more rotationally asymmetric surfaces and perform a specific optical functionality. These components are used in a wide

range of applications, such as imaging [56-60], beam shaping and illumination [61-66], and EDoF (as stated previously) [14, 38-43, 49-52]. Implementation of the static freeform components enables more compact and higher performing optical systems. However, the static freeform designs are highly dependent on the optical system characteristics, requiring specific component designs for each optical system.

In comparison, dynamic freeform optics consist of a pair of transmissive freeforms, that enable tunable optical functionality through relative movement (rotation or translation) between the two components. The relative movement between the freeform pair creates a composite wavefront with variable functionality and have been investigated in a variety of applications, including variable focus systems [67-74], tunable illuminators and beam shapers [75-79], and aberration correction [80-82]. Figure 1-3 shows the concept for an early example of variable focus lens, which was introduced independently by Alvarez [67] and Lohmann [68]. In this application, two 3<sup>rd</sup> order XY-polynomial surfaces are translated along the x-axis to create converging or diverging wavefronts depending on the direction of relative shift  $d$ , with no optical power at zero shift.

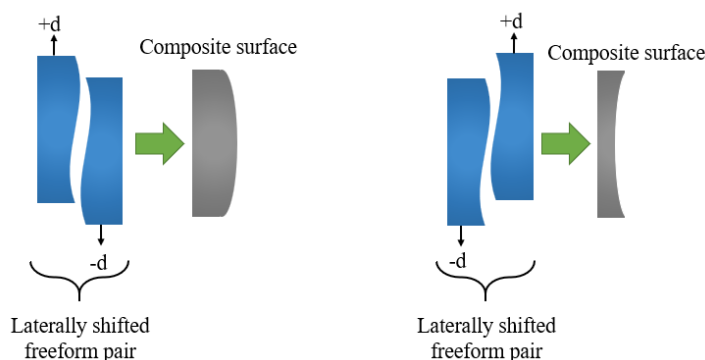


Figure 1-3: Variable power lenses using a pair of shifted freeform surfaces.

### 1.3 Freeform Optical Systems for Variable EDoF Imaging

As discussed earlier, researchers have previously investigated the design of static freeform phase plates for enabling EDoF [14, 38-43, 49-52]. However, due to the high sensitivity of these phase plates to system parameters, it is particularly interesting to investigate methods for providing tunable EDoF for multiple imaging systems.

Variable EDoF can be achieved using dynamic freeform optics by leveraging the relative rotation [83-85] or translation [86-91] of a conjugate phase plate pair. The performance of the optical system with the phase plate pair is related to the transmission function of the phase masks in these examples [92].

This dissertation, is focused on the design, implementation, and characterization of variable EDoF phase plate pairs. We use a novel approach that starts with the design and optimization of fixed freeform phase plates with cubic and logarithmic surface profiles to enable EDoF for three different imaging lenses. Variable EDoF phase plate pairs are designed using both numerical and analytical design approaches [80, 93] and their performance is compared. Variable EDoF phase plates are also fabricated and characterized experimentally.

### 1.4 Dissertation Outline

Chapter 2 introduces the design of a freeform phase plate pair with 4<sup>th</sup> order XY-polynomial surface descriptions using an analytical method [80] to enable variable EDoF imaging [94]. Three fixed Cubic Phase Plates (CPP) are designed for three commercial aspheric singlets with varying NA values. The merit function for these designs aims to maximize MTF values at specific spatial frequencies and minimize MTF differences at

selected spatial frequencies through focus. The three CPPs are then replaced by a single freeform Quartic Phase Plate Pair (QPPP) to enable EDoF for all three lenses via lateral translation of the components along the x-axis. Ray- and wave-based optical models of through-focus imaging are used to demonstrate that QPPP can enable EDoF for lenses with a range of NA values.

Chapter 3 builds on the work from Chapter 2 by considering EDoF phase plates based on logarithmic surface forms [95]. These Logarithmic Phase Plates (LPP) have previously been reported to enable EDoF over a wider defocus range than the CPP studied in Chapter 2 [50]. As with Chapter 2, three LPPs with the same merit function are designed for three aspheric lenses. Then, using a new numerical approach [93], the required freeform surfaces for a Variable Logarithmic Phase Plate Pair (VLPPP) are determined to enable EDoF for all three lenses via relative phase plate pair translation along the x-axis. The results of this study showed that LPP and VLPPP have similar through-focus performance compared to the previously designed CPP and QPPP [94].

Chapter 4 reports on the fabrication and experimental performance characterization of the CPPs and QPPPs introduced in Chapter 2. The article presents the manufacturing of CPPs, QPPPs, and optomechanical fixturing, as well as experimental measurements using a Point Source Microscope (PSM) to characterize the performance of the 0.33 NA lens with and without the EDoF phase plates. Experimental results are compared with theoretical predictions discussed in Chapter 2. The performance characterization demonstrates that the phase plates generate through-focus spots with reduced defocus sensitivity at the expense of overall performance, which is consistent with the literature., and that freeform design concepts can be used to enable variable EDoF imaging.

Lastly, Chapter 5 summarizes the results provided in Chapters 2 through 4 and compares the differences in variable EDoF design methods, their through-focus performance, optical and optomechanical manufacturing, and use of a PSM to characterize the performance of the designed phase plates. Suggestions for future research are also presented.

## CHAPTER 2: FREEFORM OPTICS FOR VARIABLE EXTENDED DEPTH OF FIELD IMAGING [93]

### 2.1 Abstract

Imaging depth of field is shallow in applications with high magnification and high numerical aperture, such as microscopy, resulting in images with in- and out-of-focus regions. Therefore, methods to extend depth of field are of particular interest. Researchers have previously shown the advantages of using freeform components to extend depth of field, with each optical system requiring a specially designed phase plate. In this paper we present a method to enable extended depth-of-field imaging for a range of numerical apertures using freeform phase plates to create variable cubic wavefronts. The concept is similar to an Alvarez lens which creates variable spherical wavefronts through the relative translation of two transmissive elements with XY polynomial surfaces. We discuss design and optimization methods to enable extended depth of field for lenses with different numerical aperture values by considering through-focus variation of the point spread function, and compare on- and off-axis performance through multiple metrics.

### 2.2 Introduction

Improving the quality of optical imaging systems is an ongoing goal of researchers. Performance criteria for image quality vary with the type of imaging systems and their applications. As one example, the lateral resolution in an imaging system can be quantified using the Rayleigh resolution criterion, defined as the minimum lateral distance,  $l$ , that can be resolved by the imaging system:

$$l = \frac{0.61\lambda}{NA}, \quad (2.1)$$

where  $\lambda$  is the source wavelength, and NA is the Numerical Aperture of the system [1]. Thus, imaging systems with higher NA values enable better lateral resolution. However, as the lateral resolution improves with higher NA, the system's depth of field degrades. Depth of field is the range of object distances from which the imaging system can create an acceptably in-focus image. This range of object distances map to a corresponding range of image-plane locations, with consequent defocus blur arising from longitudinal displacement of the observation plane with respect to the best-focus image plane. The range of image distances for which the defocus blur spot size is less than or equal to the diffraction blur is defined as the depth of focus (DoF) [1]:

$$DoF = \frac{2n\lambda}{NA^2}, \quad (2.2)$$

Strictly speaking, DoF is the image-space depth of focus, corresponding to depth of field in object space. Typical nomenclature in the community often refers to DoF as depth of field, and we follow that convention here.

In microscopy, different methods have been introduced to enable an Extended Depth of Field (EDoF) while maintaining a high NA for better lateral resolution. The confocal scanning microscope increases DoF by scanning the object with focused light along the optic axis, creating an in-focus image [2]. Wavefront coding is another technique to enable EDoF and provides the basis for this work [3]. In wavefront coding, a specially designed optical component is placed at the pupil of the imaging system to alter the Point-Spread Function (PSF) of the system and decrease its sensitivity to defocus. As a result, a blurry

intermediate image of the object is created, and then deconvolution methods are used to retrieve an image with higher quality using the known PSF (Fig. 2-1). For example, logarithmic aspheres [4], axicons [5, 6], deformable mirrors [7], annular tiered phase masks [8, 9], and binary phase modulated pupil masks [10] have been used to enable EDoF in imaging systems.

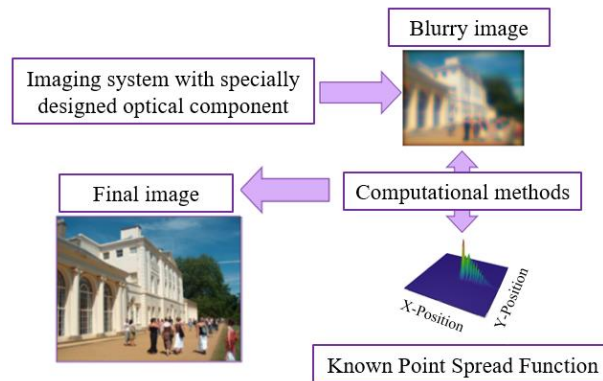


Figure 2-1: Schematic of immediate (blurry) and final (in-focus) images (using the “demo picture” provided for the image simulation in Zemax OpticStudio™), created by an imaging system with EDoF phase plate.

With recent advances in design, fabrication, and metrology of freeform optics [11], rotationally asymmetric phase masks for wavefront coding have been used more widely in imaging applications. Examples include cubic [3, 12-15] and logarithmic [16, 17] phase plates. Figure 2-2 shows examples of through-focus spots for a 0.33 NA aspheric lens with and without a cubic phase plate at  $\lambda = 633$  nm. The addition of the phase plate enables EDoF, by creating a PSF that is larger but less sensitive to defocus.

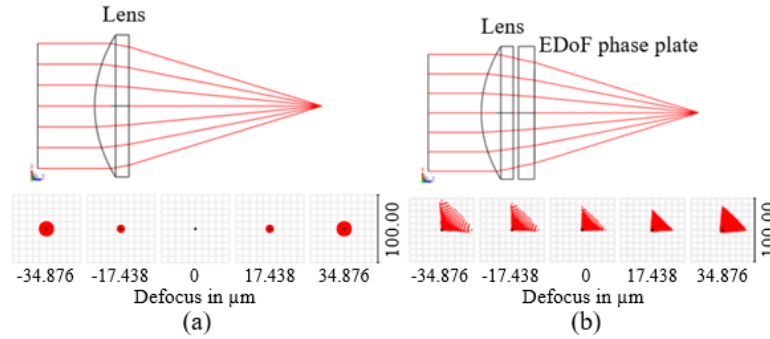


Figure 2-2: Through-focus spot diagrams for 0.33 NA aspheric lens: (a) without and (b) with a cubic phase plate. The diffraction-limited spot size and location is indicated by the black spot in each diagram.

Imaging systems with specific DoF requirements and NA values require individual phase plates. Therefore, phase masks that enable EDoF for multiple NA values can be beneficial by reducing the number of optical components, potentially reducing weight and cost. It has been previously demonstrated that one pair of phase plates can extend DoF for multiple systems by relative rotation or translation of the phase components. For example, two asymmetric phase masks with cubic polynomial surfaces were shown to extend an imaging system's DoF by creating a focus-invariant PSF through relative rotation of the phase masks [18]. Another example utilizes a pair of translated polynomial phase plates in a miniature multi-modal microscope to enable imaging different object distances mapping to the same image plane [19]. In these examples, the need to design and implement multiple fixed phase plates is eliminated by using a pair of transmissive phase plates that create a variable functionality through relative movement of the phase components. This concept is the basis of the Alvarez lens design [20], which is a variable focus lens composed of two identical, laterally shifted (along the  $x$ - or  $y$ -axes) freeform components with an XY polynomial surface equation. The focusing power of the composite surface generated by the freeform elements changes with the relative translation between the pairs. Such shifted

optical components that create variable functionality have been used for multiple additional applications, including aberration correction [21, 22], beam shaping [23, 24], and head-mounted displays [25].

In this paper we propose a design method for a freeform phase plate pair that enhances DoF for multiple lenses with different NA values through lateral relative translation of the phase plates along the  $x$ -axis. We examine the DoF extension both qualitatively and quantitatively by considering through-focus variation of (1) ray-traced spot diagrams, and (2) diffraction-based PSF models, respectively. Researchers have previously reported focus-invariant systems through relative shifts of equal amounts along both the  $x$ - and  $y$ -axes between a pair of phase plates with surface profiles given by:

$$z(x, y) = k(x^4 + y^4), \quad (2.3)$$

where  $k$  denotes the strength of the phase plate [26]. This approach is similar to the use of shifted freeform components along both axes for a variable-focus effect [27]. However, the basis for choosing this surface equation is not discussed, and the optimization method and criteria for determining the optimum  $k$  coefficient value are not reported [26].

For our approach, we consider multiple lenses with different NA values. We first design fixed Cubic Phase Plates (CPP), one for each lens, that enable EDoF using an optimization method based on the Modulation Transfer Function (MTF). Each phase plate is a plano-freeform, with the equation of the freeform surface given by:

$$z(x, y) = \alpha(x^3 + y^3), \quad (2.4)$$

where the value of the cubic coefficient  $\alpha$  depends on the corresponding lens NA and the optimization parameters. The resulting fixed phase plates are then replaced by one pair of phase plates with a 4<sup>th</sup> order (quartic) surface description that enable EDoF for all the lenses and NA values. Relative shifts between the quartic freeform pair create composite surfaces with similar functionality to the fixed cubic phase plates, as illustrated in Figure 2-3.

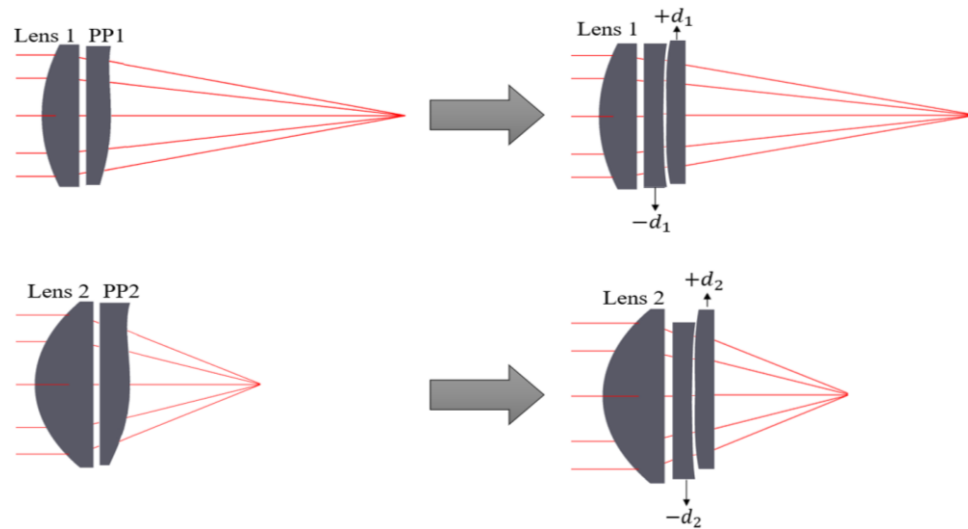


Figure 2-3: Representative images of the EDoF systems considered in this manuscript. Two fixed Phase Plates (PP1 and PP2) may be replaced with one pair of freeform phase plates to enable EDoF through the relative translation of the phase plates along the x-axis.

## 2.3 Design approach

### 2.3.1 Variable phase plate design

Consider a pair of plano-freeform elements with and without relative shifts between the surfaces, as illustrated in Figure 2-4:

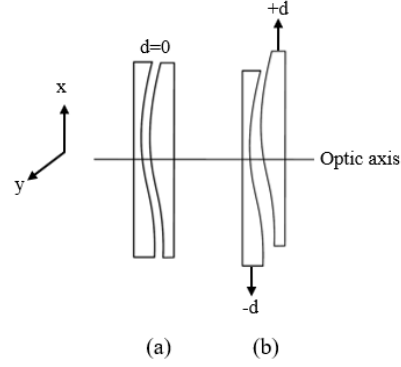


Figure 2-4: Schematic of a pair of plano-freeform components (a) with no lateral shift and (b) with shifts along the  $x$ -axis of equal amount and opposite direction.

There is no optical functionality at zero shift, but variable optical functionality is introduced to the system as the components are translated along the  $x$ -axis by amounts  $d$  in opposite directions, as shown. For this work, the goal is to obtain the same functionality of the cubic surface described in Eq. (2.4) where the value of the  $\alpha$  coefficient is tuned by changing the shift  $d$  between the two freeform plates. For small values of  $d$ , we can apply a method introduced by Palusinski [21], to show that:

$$z_f(x, y) \propto \int z(x, y) dx, \quad (2.5)$$

where  $z_f(x, y)$  is the general equation for each freeform surface in the pair. Eqs. (2.4) and (2.5) are then used to obtain:

$$z_f(x, y) = \beta \left( \frac{x^4}{4} + xy^3 \right), \quad (2.6)$$

where

$$\beta = \frac{\alpha_{\max}}{2d_{\max}(n-1)}, \quad (2.7)$$

In Eq. (2.7),  $\alpha_{max}$  is the cubic coefficient for the highest NA lens considered,  $d_{max}$  is the maximum desired shift between the phase plates, and  $n$  is the refractive index of the phase plate material at the design wavelength. This equation is derived considering the composite wavefront resulting from transmission through the shifted phase plate pair and its relation to the cubic phase plate coefficient for the highest NA lens. After calculating  $\beta$ , the relative shifts needed for lenses with lower NA values are calculated, using Eq. (2.8):

$$d = \frac{\alpha}{2\beta(n-1)}, \quad (2.8)$$

where  $\alpha$  is the optimized cubic coefficient for each lens, and  $\beta$  is calculated using Eq. (2.7). We refer to the pair of components for variable EDoF with surfaces described by Eq. (2.6) as a Quartic Phase Plate Pair (QPPP) in the following discussion.

### 2.3.2 Optical design and optimization

We consider three commercial aspheric singlets with 22.5 mm clear aperture and NA values of 0.25, 0.33, and 0.5 respectively as the basis for design of the example EDoF phase plates [28]. The EDoF phase plates are all assumed to be made of Polymethyl Methacrylate (PMMA) with a 22 mm clear aperture, 3 mm thickness, and design wavelength of 633 nm, giving a refractive index of 1.489. Simulation and optimization were performed in Zemax OpticStudio™ and imported into MATLAB™ and Excel™ for formatting and presentation where appropriate. Three CPP's, one for each lens, were designed to enable EDoF. For better performance, it is necessary to place the phase plates at or near the exit pupil of the imaging system. However, due to inaccessibility of the exit pupils for the selected lenses

and optomechanical considerations for the test setup, the air gaps between the aspheric lenses and phase plates are set to 1 mm. The design goal is to create spots with less sensitivity to defocus over a targeted axial range from  $-6\Delta z$  to  $+6\Delta z$ , with  $\Delta z$  given by:

$$\Delta z = \frac{DoF}{2}, \quad (2.9)$$

where DoF is calculated using Eq. (2.2). The cubic coefficient  $\alpha$  is optimized for each lens for image planes located at integer multiples of  $\Delta z$  across the target range. The optimization follows two main goals: (1) improving the system's overall performance by increasing through-focus MTF values at specific spatial frequencies, and (2) achieving more consistent through-focus performance by minimizing differences between the through-focus MTF values for the selected frequencies.

The optimization frequencies were selected by identifying the specific frequency ranges exhibiting low values in the through-focus MTF performance of each lens. This criterion can be directly implemented in the merit function within the design software and enables control of specific performance requirements. After selecting the spatial frequencies demonstrating this behavior, the phase plate parameters were optimized to increase the MTF and minimize the through-focus MTF variation for each lens. Table 2-1 summarizes the spatial frequencies selected for optimization for each lens.

Table 2-1: Optimization frequencies used to design EDoF phase plates for the selected aspheric lenses.

Lens NA	Optimization spatial frequencies (cycles/mm)
0.25	60, 86, 124, 240
0.33	61, 98, 115, 270
0.5	80, 160, 320, 480

After optimizing the  $\alpha$  coefficient for each lens, the  $\beta$  coefficient for the QPPP is calculated ( $\beta=9.205 \times 10^{-6}$ ) using the EDoF requirement for the highest NA lens ( $\alpha_{max}$ ) and desired maximum shift amount ( $d_{max} = 2$  mm) following Eq. (2.7). The air gap between the aspheric lens and first QPPP element is also set to 1 mm. The spacing between the first and second QPPP components is set to 400  $\mu\text{m}$  to avoid collisions between the shifted parts and considers their overall sag over the full diameter, as well as manufacturing and optomechanical mounting constraints. Figure 2-5 shows the CPP surface for the 0.33 NA lens and one of the resulting QPPP surfaces.

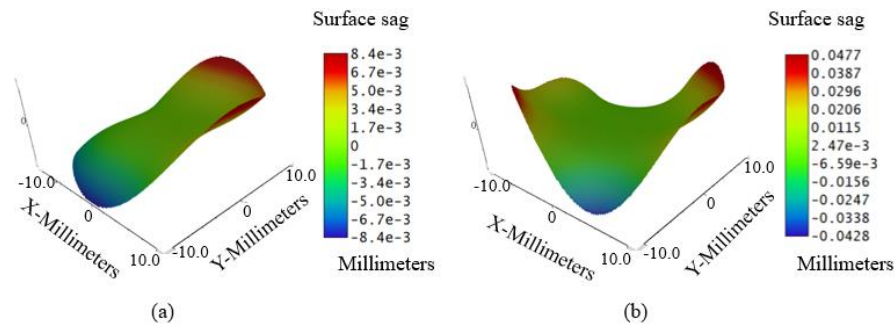


Figure 2-5: (a) Surface of designed CPP for 0.33 NA lens and (b) surface of one of the quartic phase plates.

## 2.4 Design results

### 2.4.1 Cubic Phase Plate (CPP) designs

Three CPP's were designed based on the criteria discussed in Sec. 2.2. Each of these phase plates enables EDoF for the selected lenses with specific NA values. Table 2-2 summarizes the optimization results for the designs. The cubic coefficients and the surface sags of the phase plates increase as the numerical aperture of the system increases.

Table 2-2: Cubic phase plate optimization results.

Lens NA	$\Delta z$ ( $\mu\text{m}$ )	Optimized $\alpha$	Phase plate sag ( $\mu\text{m}$ )
0.25	10.1	$2.473 \times 10^{-6}$	8.6
0.33	5.8	$6.317 \times 10^{-6}$	21.9
0.5	2.5	$1.804 \times 10^{-5}$	62.4

#### 2.4.2 Quartic Phase Plate Pair (QPPP) designs

One pair of variable phase plates with  $\beta = 9.205 \times 10^{-6}$  (as derived in Section 2.3.2) was used to replace the three CPP's through relative translation of the phase components along the  $x$ -axis. Table 2-3 summarizes the relative shift of each element in the QPPP systems needed for each lens NA.

Table 2-3: Quartic phase plate pair design results.

Lens NA	$\Delta z$ ( $\mu\text{m}$ )	Relative phase plate shift (mm)	Phase plate sag ( $\mu\text{m}$ )
0.25	10.1	0.269	90
0.33	5.8	0.700	
0.5	2.5	2.000	

## 2.5 Performance Comparisons

### 2.5.1 On-axis system performance

#### 2.5.1.1 Through-focus spot diagrams

Figure 2-6 qualitatively compares through-focus ( $-6\Delta z$  to  $+6\Delta z$ ) spot diagrams for the selected lenses when used with the respective CPP's and QPPP. As expected, the addition of the EDoF phase plates results in an increase in the through-focus spot size but reduced variation in spot size through the defocus range. The spots for the QPPP are notably larger than those obtained for the CPP. We make more quantitative performance comparisons below.

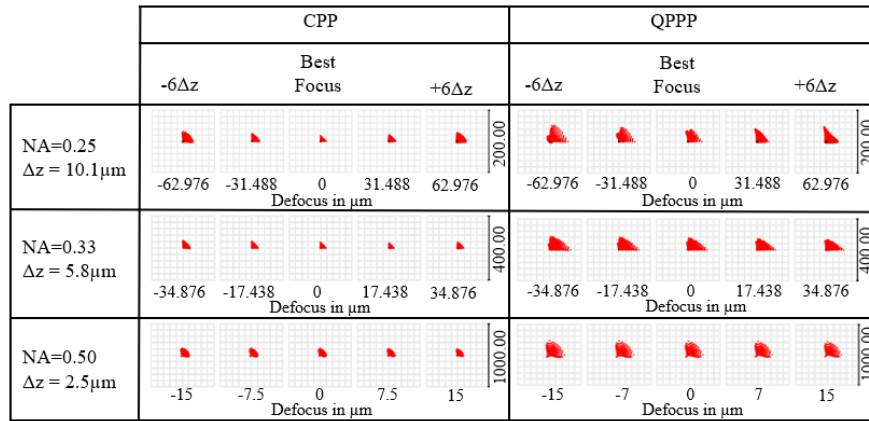


Figure 2-6: Through-focus spot diagrams for the three aspheric lenses with fixed CPP's and variable QPPP.

### 2.5.1.2 Through-focus MTF

As discussed previously, the addition of EDoF phase plates enables more consistent through-focus spots at the expense of lower system performance. The primary objectives for designing the cubic and quartic phase plates are to increase through-focus MTF at the selected frequencies and to achieve more consistent through-focus performance by minimizing the through-focus MTF differences at the selected spatial frequencies. We observe that adding the EDoF phase plates worsens the on-axis system MTF at the best image plane for both the CPP and QPPP, as shown in Figure 2-7.

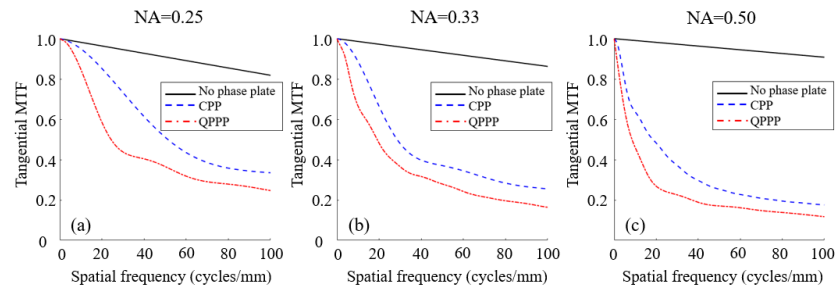


Figure 2-7: Tangential MTF at the best focus for the (a) 0.25, (b) 0.33, and (c) 0.50 NA lenses with and without EDoF phase plates.

Figure 2-8 compares the on-axis through-focus MTF values for the 0.25, 0.33, and 0.5 NA lenses with and without EDoF phase plates at 80 cycles/mm as an example. The MTF varies less through focus ( $-6\Delta z$  to  $+6\Delta z$ ) with the addition of the phase plates, though the peak MTF values are lower, as expected.

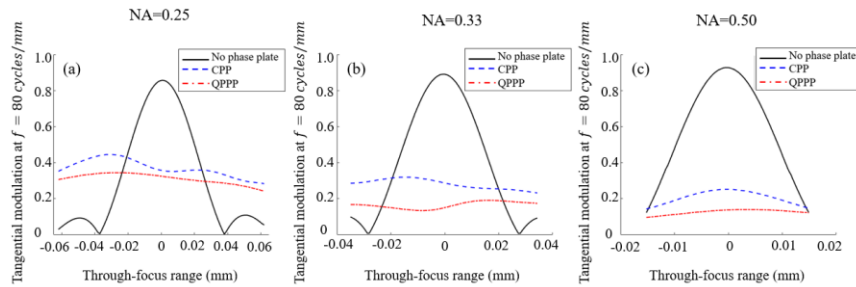


Figure 2-8: On-axis through-focus tangential MTF plots for the (a) 0.25, (b) 0.33, and (c) 0.50 NA lenses with and without EDoF phase plates at  $f = 80$  cycles/mm.

### 2.5.1.3 Root-Mean-Square (RMS) deviation and slope of RMS deviation of PSF

The PSF of an optical system shows how the system images a point source. The PSF changes as the location of the observation plane varies from the best image plane. Figure 2-6 qualitatively shows how the through-focus spots vary for the selected lenses when used with the respective phase plates. For more quantitative comparisons, it is necessary to use diffraction-based models of the PSF. As an example, Figure 2-9 shows the normalized PSF for the 0.33 NA lens with the designed CPP at best focus and  $\pm 4\Delta z$  image plane locations. Similar normalized PSF calculations were performed for the range of lenses, phase plates, and defocus distances. The results were then used to calculate both the RMS deviation of the PSF and the slope of the RMS deviation of the PSF as quantitative measures of the through-focus variability. The expectation is that with the addition of the EDoF phase

plates, the PSF will remain consistent in shape and size through focus, resulting in lower RMS deviation values.

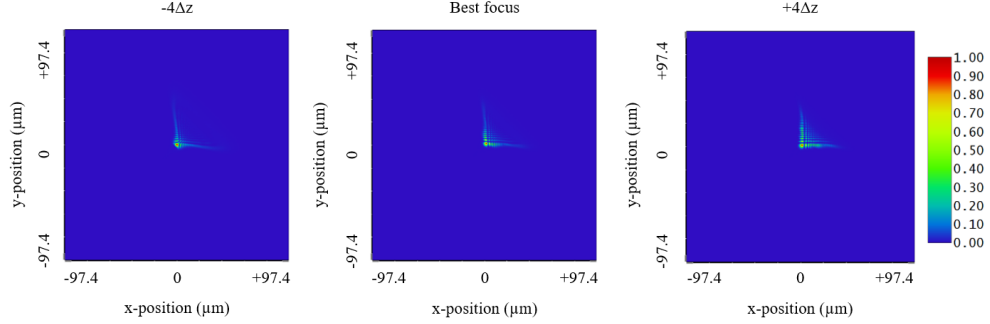


Figure 2-9: Normalized PSF for the 0.33 NA lens with CPP at best focus and  $\pm 4\Delta z$ .

To this end, the RMS deviation of PSF is calculated between the normalized PSF at best focus and the defocus image planes (point by point):

$$RMS = \sqrt{\frac{1}{m^2} \sum_{i=1}^m \sum_{j=1}^m (PSF_{d,i,j} - PSF_{f,i,j})^2}, \quad (2.10)$$

where  $m^2$  is the total number of samples in the PSF matrix and  $PSF_{d,i,j}$  and  $PSF_{f,i,j}$  represent the normalized PSF (in matrix form and  $m=1024$ ) at the defocused and best focus planes, respectively.

Variations in the RMS deviation of the PSF for a system with no EDoF phase plate are expected as the through-focus location of the image plane changes. Similarly, systems with the EDoF phase plates should have lower through-focus RMS deviation with reduced sensitivity to defocus. Figure 2-10 compares the normalized PSF RMS deviation through focus ( $-6\Delta z$  to  $+6\Delta z$ ) for each of the three lenses with different NA values with and without EDoF phase plates. For each lens, the addition of the phase plates enables a lower

RMS deviation of PSF, resulting in a more consistent through-focus performance, and the CPP's show a slightly lower PSF variance than the QPPP.

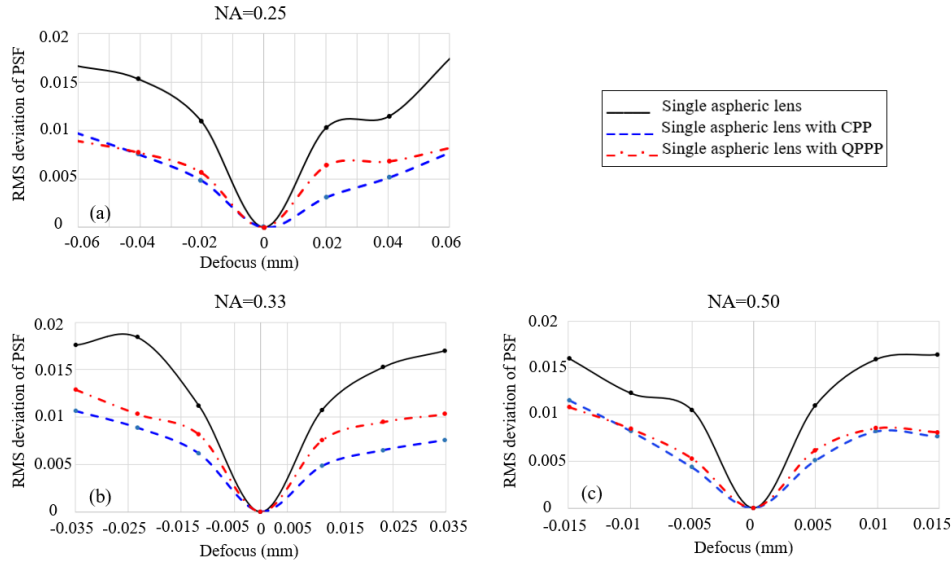


Figure 2-10: RMS deviation of PSF through focus for the (a) 0.25, (b) 0.33, and (c) 0.50 NA lenses with and without EDoF phase plates.

We also consider the slope of the RMS deviation of the PSF as another quantitative metric to compare through-focus spot variation for systems with and without the EDoF phase plates. The slope for each plot shown in Figure 2-10 represents the rate at which the RMS deviation of PSF changes and can be calculated as:

$$s_i = \frac{RMS_{i+1} - RMS_i}{d_{i+1} - d_i}, i = 1, 2, \dots, 6 \quad (2.11)$$

where  $s_i$  is the slope of the RMS deviation of PSF for each two consecutive defocus image planes, and  $RMS_{i+1}$  and  $RMS_i$  are the RMS deviations of PSF values calculated for the image planes at  $d_{i+1}$  and  $d_i$  locations respectively (from  $-6\Delta z$  to  $+6\Delta z$ ). With the addition of the designed EDoF phase plates, we expect to see a lower slope, as the phase plates

decrease the spot variation through focus. Figure 2-11 shows the slopes of the RMS deviation of PSF for the three aspheric lenses with different NA's, with and without the phase plates. The rate at which the through-focus PSF changes is lower for systems with CPP and QPPP, as expected. In addition, the difference between CPP and QPPP for each system is small, with a lower rate for CPP.

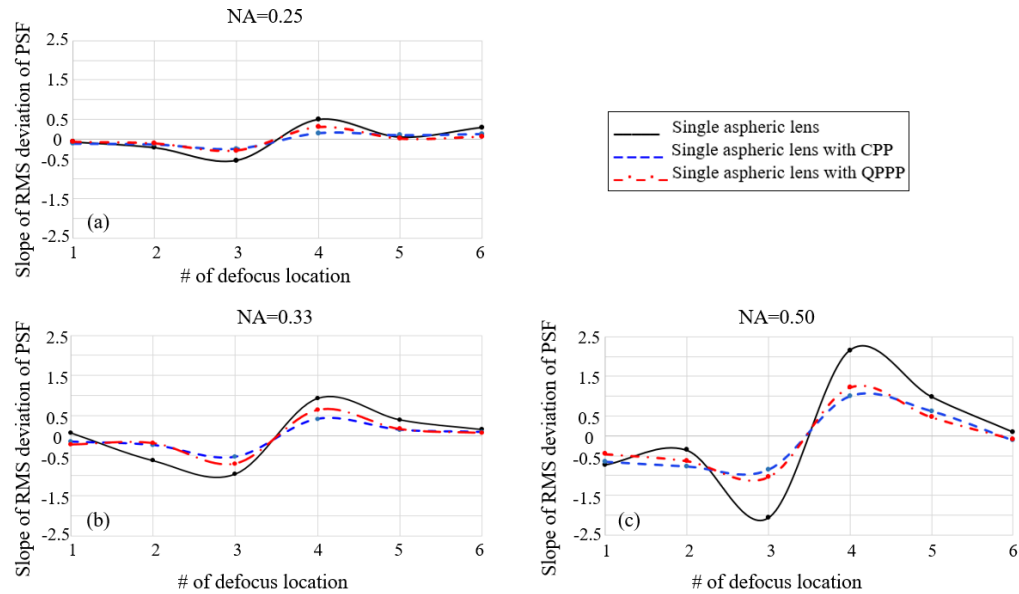


Figure 2-11: Slope of RMS deviation of PSF through focus for the (a) 0.25, (b) 0.33, and (c) 0.50 NA lenses with and without EDoF phase plates.

## 2.5.2 Off-axis system performance

### 2.5.2.1 Through-focus spot diagrams vs. field angle

For imaging applications, it is also essential to consider system performance for off-axis object locations. Figure 2-12 compares through-focus spot diagrams for the 0.33 NA asphere with the CPP and QPPP designs at 0, 1 and 3-degree field angles along the y-axis. We note that for each field angle, the spot shapes are relatively constant, while the through-

focus spot sizes change more noticeably for higher field angles, particularly for the CPP case.

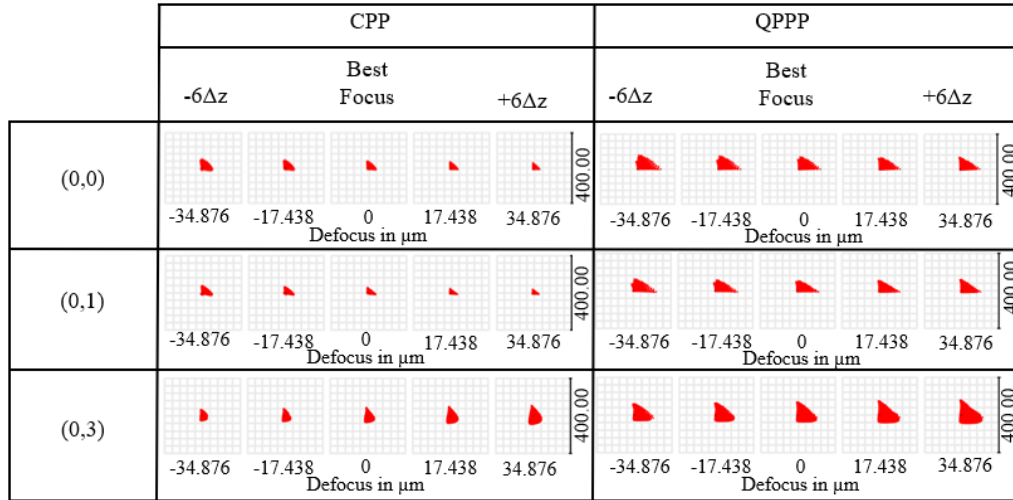


Figure 2-12: Through-focus spot diagrams for 0.33 NA lens with CPP and QPPP over 3-degree field angle range along the y-axis.

### 2.5.2.2 MTF vs. field angle

As a representative example, we compare the tangential MTF at best focus and through focus for the 0.33 NA aspheric lens with and without EDoF phase plates. Figure 2-13 shows the MTF at best focus at field angles of 0, 1 and 3-degrees along the y-axis. We observe that the MTF drops as the field angle increases for the aspheric lens by itself as well as in both EDoF systems, with a caveat that the MTF at 1-degree field angle is slightly higher than seen with on-axis light for lower spatial frequencies for the EDoF systems.

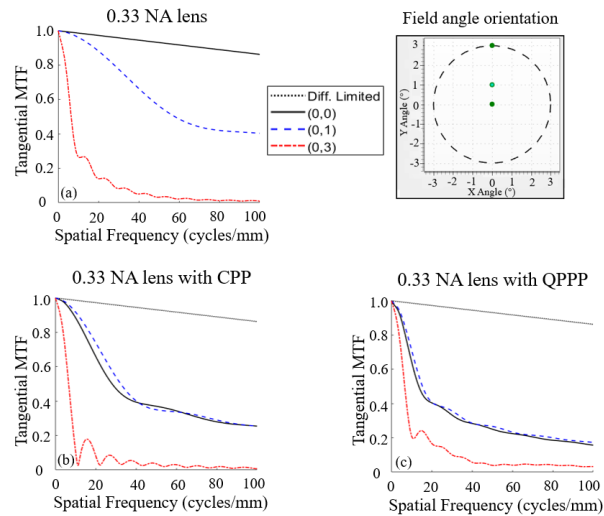


Figure 2-13: Best focus tangential MTF plots at 0,1 and 3-degree field angles along the y-axis for (a) 0.33 NA aspheric lens, and 0.33 NA lens with (b) CPP and (c) QPPP.

To examine this unexpected result more closely, we also consider the tangential MTF for 1-degree field angles at different orientations around the optical axis, as shown in Figure 2-14.

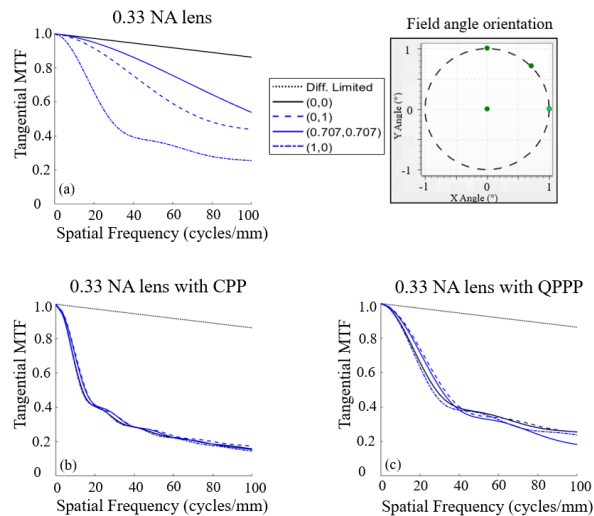


Figure 2-14: Best focus tangential MTF plots at 1-degree field angles at different orientations around the optical axis for (a) 0.33 NA aspheric lens, and the same lens with (b) CPP and (c) QPPP.

From Figure 2-14 we observe that the relative MTF of all the systems (with and without EDoF phase plates) are sensitive to both field angle and the orientation of the field point around the optical axis. The systems containing EDoF phase plates appear to be less sensitive to orientation than the lens alone, though at the cost of reduced image contrast. The results observed in both Figure 2-13 and Figure 2-14 for both fixed CPP and variable QPPP are consistent with prior research showing decreased field angle sensitivity with static cubic phase plates [13].

As an additional example, Figure 2-15 shows through-focus modulation (tangential) values at the lowest spatial frequency used for CPP design (61 cycles/mm) for the 0.33 NA aspheric lens, with and without the designed CPP and QPPP at 0, 1 and 3-degree field angles (along the y-axis). While the absolute results would vary as a function of the chosen spatial frequency, the modulation values for the systems containing EDoF phase plates are more consistent through focus (particularly for smaller field angles) than the lens alone, but again at the cost of reduced image contrast that worsens with increased field angle.

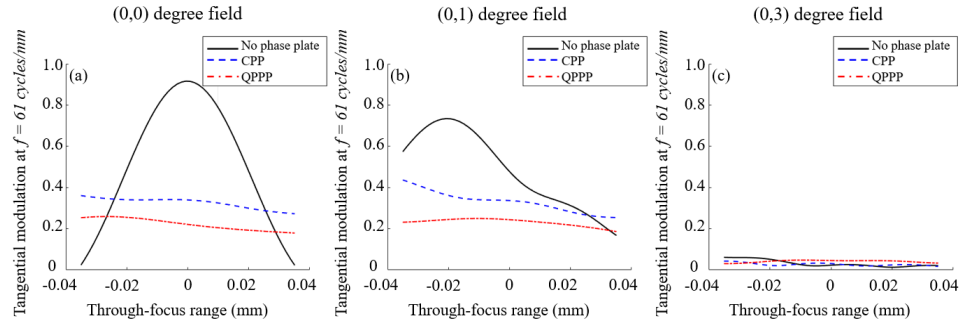


Figure 2-15: Through-focus tangential modulation plots for 0.33 NA aspheric lens with and without EDoF phase plates at (a) 0, (b) 1, and (c) 3-degree field angle at  $f = 61$  cycles/mm.

## 2.6 Discussion and Conclusion

We have proposed a design method to enable variable extended depth of field imaging using a pair of transmissive freeform phase plates. First, we designed three fixed CPP's for commercial aspheric singlets with different numerical apertures using an on-axis MTF-based optimization method. The optimization routine was implemented to improve each system's MTF while decreasing the through-focus MTF variation. Multiple CPP's were then replaced by one QPPP to enable multiple focus-invariant systems. This approach can decrease the number of parts needed to enable EDoF imaging for multiple systems and potentially reduce system costs.

The RMS deviation of PSF, and its slope, were proposed and calculated for the CPP and QPPP systems as quantitative metrics for through-focus variation. The RMS deviation and slope deviation of PSF for systems with CPP's and QPPP are lower than for a corresponding lens with no phase plate, illustrating the reduced through-focus variation that is desirable for an EDoF system. While the overall performance of the QPPP system in terms of spot size and PSF variability is generally lower than for the corresponding CPP systems, the QPPP still can serve as a suitable replacement for multiple CPP elements. We

believe the difference in CPP and QPPP performance can be attributed to the air gap needed between the two phase plates in the QPPP systems, and the fact that the CPP elements are specifically optimized while the QPPP design is derived from the CPP elements, rather than optimized.

We compared on- and off-axis performance of fixed CPP's and variable QPPP for a range of numerical apertures. The through-focus spot diagrams showed that the CPP's and QPPP enable spots with less through-focus variation compared to systems without phase plates, with an increase in the spot sizes and reduction in the MTF for QPPP systems relative to the CPP systems. Comparisons also showed that the performance of both CPP's and QPPP decrease at higher field angles. Results from on- and off-axis fields demonstrate the sensitivity of EDoF phase plates to increasing field angles and their directionality. These sensitivities may also be attributable to asymmetries in the phase plates surfaces and the directionality of the shifts between the QPPP elements. These factors suggest the need for additional study of (1) phase plates with more design freedoms, (2) optimization methods that consider off-axis field angles, and (3) analyses based on the 2D MTF and recent related performance metrics such as the Minimum Modulation Curve [29].

Work is currently underway on fabricating the designed phase plates (CPP's and QPPP) for experimental performance characterization and comparison to theoretical predictions.

## 2.7 References

1. T. S. Tkaczyk, *Field Guide to Microscopy* (SPIE, 2010) p.41.
2. M. Minsky, "Microscopy Apparatus," U.S patent application 3,013,467 (1961).

3. E. R. Dowski, and W. T. Cathey, "Extended depth of field through wave-front coding," *Appl. Opt.* **34**, 1859-1866 (1995).
4. W. Chi, and N. George, "Electronic imaging using a logarithmic asphere," *Opt. Lett.* **26**, 875-877 (2001).
5. Z. Zhai, S. Ding, Q. Lv, X. Wang, and Y. Zhong, "Extended depth of field through an axicon," *Journal of Modern Optics* **56**, 1304-1308 (2009).
6. R. N. Zahreddine, and C. J. Cogswell, "Total variation regularized deconvolution for extended depth of field microscopy," *Appl. Opt.* **54**, 2244-2254 (2015).
7. W. J. Shain, N. A. Vickers, B. B. Goldberg, T. Bifano, and J. Mertz, "Extended depth-of-field microscopy with a high-speed deformable mirror," *Opt. Lett.* **42**, 995-998 (2017).
8. K. Chu, N. George, and W. Chi, "Extending the depth of field through unbalanced optical path difference," *Appl. Opt.* **47**, 6895-6903 (2008).
9. S. Abrahamsson, S. Usawa, and M. Gustafsson, "A new approach to extended focus for high-speed high-resolution biological microscopy," *Proc. SPIE* **6090**, 60900N (2006).
10. R. N. Zahreddine, and C. J. Cogswell, "Binary phase modulated partitioned pupils for extended depth of field imaging," in *Imaging and Applied Optics (2015)* p. IT4A.2.
11. J. P. Rolland, M. A. Davies, T. J. Suleski, C. Evans, A. Bauer, J. C. Lambropoulos, and K. Falaggis, "Freeform optics for imaging," *Optica* **8**, 161-176 (2021).
12. M. Demenikov, and A. R. Harvey, "Image artifacts in hybrid imaging systems with a cubic phase mask," *Opt. Express* **18**, 8207-8212 (2010).

13. G. Muyo, A. Singh, M. Andersson, D. Huckridge, A. Wood, and A. R. Harvey, "Infrared imaging with a wavefront-coded singlet lens," *Opt. Express* **17**, 21118-21123 (2009).
14. S. Prasad, T. Torgersen, V. Pauca, R. Plemmons, and J. van der Gracht, "Engineering the pupil phase to improve image quality," *Proc. SPIE* **5108**, pp. 1-12 (2003).
15. M. Somayaji, V. R. Bhakta, and M. P. Christensen, "Experimental evidence of the theoretical spatial frequency response of cubic phase mask wavefront coding imaging systems," *Opt. Express* **20**, 1878-1895 (2012).
16. S. S. Sherif, W. T. Cathey, and E. R. Dowski, "Phase plate to extend the depth of field of incoherent hybrid imaging systems," *Appl. Opt.* **43**, 2709-2721 (2004).
17. H. Zhao, Q. Li, and H. Feng, "Improved logarithmic phase mask to extend the depth of field of an incoherent imaging system," *Opt. Lett.* **33**, 1171-1173 (2008).
18. M. Demenikov, G. Muyo, and A. R. Harvey, "Experimental demonstration of continuously variable optical encoding in a hybrid imaging system," *Opt. Lett.* **35**, 2100-2102 (2010).
19. S. S. Rege, T. S. Tkaczyk, and M. R. Descour, "Application of the Alvarez-Humphrey concept to the design of a miniaturized scanning microscope," *Opt. Express* **12**, 2574-2588 (2004).
20. L. W. Alvarez, "Two-element variable-power spherical lens," U.S patent 3,305,294 (1967).
21. I. A. Palusinski, J. M. Sasián, and J. E. Greivenkamp, "Lateral-shift variable aberration generators," *Appl. Opt.* **38**, 86-90 (1999).

22. T. Mitchell, and J. Sasian, "Variable aberration correction using axially translating phase plates," Proc. SPIE **3705**, pp. 209-220 (1999).
23. P. J. Smilie, and T. J. Suleski, "Variable-diameter refractive beam shaping with freeform optical surfaces," Opt. Lett. **36**, 4170-4172 (2011).
24. T. J. Suleski, J. Shultz, and P. Smilie, "Dynamic beam shaping with freeform optics," Proc. SPIE **9194**, 91940K (2014).
25. A. Wilson, and H. Hua, "Design and demonstration of a vari-focal optical see-through head-mounted display using freeform Alvarez lenses," Opt. Express **27**, 15627-15637 (2019).
26. T. Hellmuth, A. Bich, R. Börret, A. Holschbach, and A. Kelm, "Variable phaseplates for focus invariant optical systems," Proc. SPIE **5962**, 596215 (2005).
27. A. W. Lohmann, "A New Class of Varifocal Lenses," Appl. Opt. **9**, 1669-1671 (1970).
28. "Edmund Optics," <https://www.edmundoptics.com/f/precision-aspheric-lenses/13139>.  
Part numbers: 33-945, 49-104, and 49-102.
29. H. Aryan, G. D. Boreman, and T. J. Suleski, "The Minimum Modulation Curve as a tool for specifying optical performance: application to surfaces with mid-spatial frequency errors," Opt. Express **27**, 25551-25559 (2019).

## CHAPTER 3: PSF ENGINEERING WITH VARIABLE LOGARITHMIC PHASE PLATES FOR EXTENDED DEPTH OF FIELD [95]

### 3.1 Abstract

Shallow depth of field in imaging systems with high numerical apertures results in images with in- and out-of-focus regions. Therefore, methods to enhance the depth of field are of special interest. In point spread function engineering, a custom phase plate is designed for each system to reduce sensitivity to defocus and thereby extend depth of field. In this paper, we present a method that enables extended depth of field for a range of numerical apertures using a freeform variable logarithmic phase plate pair. We leverage a numerical design approach for the variable phase plate pair design, and explore phase plate optimization and performance by quantifying and comparing through-focus point spread function variation, and on- and off-axis performance for the designed phase plates.

### 3.2 Introduction

The minimum lateral distance that an optical imaging system can resolve (the Rayleigh resolution) is inversely proportional to system Numerical Aperture (NA) [1], and the axial distance in object space over which the optical system creates an in-focus image of the object, the Depth of Field (DoF), is inversely proportional to the square of NA [2]. With increases in system NA and magnification, the lateral resolution is improved while the DoF becomes shallow; therefore, methods that enable Extended DoF (EDoF) while maintaining system NA are beneficial. DoF is defined in the object space, but the expression has been

used to study spot and Point-Spread Function (PSF) variation in the image space (depth of focus), and we follow similar terminology throughout this work.

PSF engineering has provided powerful methods to modify transmitted wavefronts to reduce sensitivity to defocus and thus enable EDoF [3]. In PSF engineering, a custom phase component is placed at or near the system exit pupil and computational methods are then used to retrieve sharper images. A wide range of phase elements with rotationally symmetric [4–11] and asymmetric [12–20] surface profiles have previously been used to enable EDoF. For these applications, a specially designed component is required for each system. Thus, methods with the potential to enable EDoF for multiple imaging systems with the same phase element or elements can be advantageous.

The concept of creating variable wavefronts through relative movement between two identical components has been previously reported for multiple applications, including variable power lenses [21–26], aberration correction [27–29], tunable illuminators [30] and beam shaping [31,32], among others. For variable EDoF, the two phase plates are translated or rotated relative to each other to create a focus-invariant PSF. Examples include shifted and rotated polynomial, sinusoidal, hyperbolic and gaussian mask pairs for applications such as barcode readers, microscopy and 3D imaging [33–40].

We have previously reported on the design of Quartic Phase Plate Pairs (QPPP) to enable EDoF for aspheric singlets with different NA values [41] based on Cubic Phase Plate (CPP) designs [42]. In this approach, fixed CPPs were designed for the selected lenses and then an analytical approach [27] was used to derive the surface equation and calculate the surface coefficient of the QPPP and the required shifts to match the NA for each lens.

Logarithmic Phase Plates (LPP) have been previously reported to enable EDoF over larger ranges of defocus compared to CPP [13]. This result provides motivation for our study on the design and performance of Variable Logarithmic Phase Plate Pairs (VLPPP) to further extend DoF for lenses with different NA values through relative translation of VLPPP components, in a manner analogous to the prior work on QPPP [42]. The general surface form of the LPP is given in Eq. (3.1) [13]:

$$z(x, y) = \text{sgn}(x)\alpha x_{\max}^2 x^2 (\log |x| + \beta) - \frac{u' x_{\max} x}{z_i} + \text{sgn}(y)\alpha y_{\max}^2 y^2 (\log |y| + \beta) - \frac{v' y_{\max} y}{z_i}, \quad (3.1)$$

In this equation,  $\alpha$  and  $\beta$  are logarithmic parameters,  $x_{\max}$  and  $y_{\max}$  are half-widths of the aperture,  $(u', v')$  is an arbitrary point in the image plane, and  $z_i$  is the image distance. The LPP and VLPPP components are plano-freeform configurations placed at or near the exit pupil of the optical system, as illustrated in Figure 3-1 for aspheric singlets.

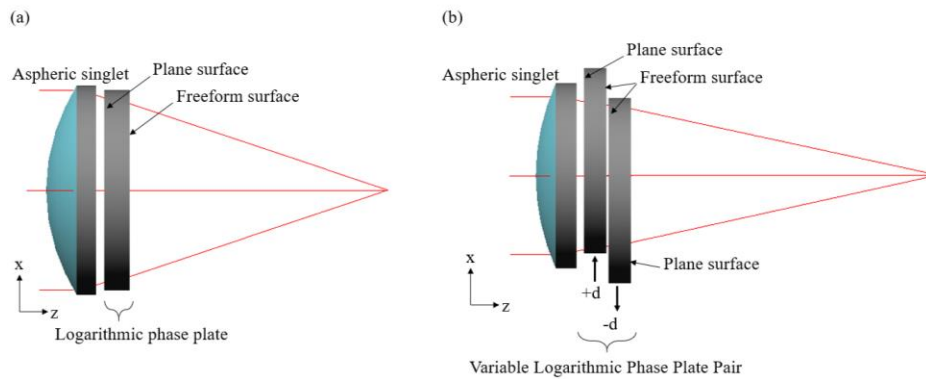


Figure 3-1: Schematic of a 0.25 NA aspheric lens with (a) LPP and (b) VLPPP.

We note that the nature of the LPP surface descriptions necessitates a different design approach than previous work from [42]. In particular, the analytical design method used to derive the form of the QPPP from CPP is not conducive for the present work on logarithmic

phase plates; as a consequence, a numerical design approach must be implemented to find the desired VLPPP surfaces [43]. We consider the EDoF capability of the resulting logarithmic phase plates by comparing both through-focus spot diagrams (ray-based models) and PSFs (wave-based models). The analyses of the LPP and VLPPP elements parallel the treatment of the CPP and QPPP systems in Ref. [42] to enable direct comparison of the two geometries.

### 3.3 Design Approach and Results

For this design, three Commercial-Off-The-Shelf (COTS) aspheric singlets with 0.25, 0.33, and 0.50 NA values and 22.5 mm Clear Aperture (CA) are considered [41]. CODE V and MATLAB were used for optical design and performance analysis. A schematic illustration of the design procedures for the LPP and VLPPP components is shown in Figure 3-2.

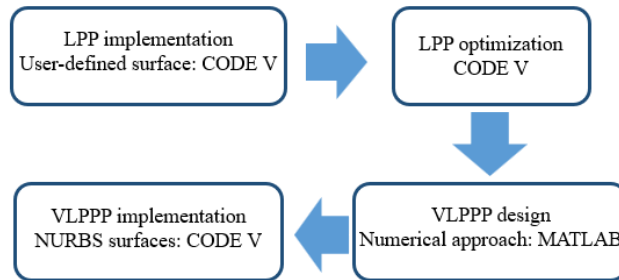


Figure 3-2: Summary of the LPP and VLPPP design process.

First, the LPP form is implemented in CODE V. CODE V supports a wide range of surface profiles for implementation, however, the logarithmic form of Eq. (3.1) is not supported and therefore, a User-Defined surface is required [44]. Next, the LPP surface coefficients are optimized in CODE V for all lenses. The LPP designs for the 0.25 and 0.50

NA lenses are then used as boundary elements in MATLAB as part of a numerical design process to realize point-cloud representations of the VLPPP elements [43]. The resulting VLPPP surface point clouds are next imported into CODE V as User-Defined NURBS surfaces, where they can be used to model the desired EDoF functionality across the range of NA values. We now consider each of these design stages in more detail.

### 3.3.1 *Logarithmic Phase Plate design and optimization*

As shown in Figure 3-1(a), the LPPs are in a plano-freeform configuration located near the exit pupil of the aspheric singlets. However, due to inaccessibility of the exit pupils for the selected lenses and optomechanical considerations, the air gaps between the aspheric lenses and phase plates were set to 1 mm. The LPPs are designed from Polymethyl Methacrylate (PMMA) at a design wavelength of 633 nm (refractive index  $n=1.489$ ) with 22 mm clear aperture and 3 mm center thickness.

The LPP was implemented in CODE V using Eq. (3.1) and its derivative to create a user-defined surface for use in optimizing the performance of the EDoF system [44,45]. The design goal is to create spots that are insensitive to defocus over a range from  $-6\Delta z$  to  $+6\Delta z$ , where:

$$\Delta z = \frac{n\lambda}{NA^2}, \quad (3.2)$$

where  $n$  is the refractive index of the surrounding medium ( $n=1$  for air),  $\lambda$  is the design wavelength and  $NA$  is the lens numerical aperture [1]. The variable parameters for the LPP

design are the  $\alpha$  and  $\beta$  coefficients in Eq. (3.1);  $u'$ ,  $v'$  and  $z_i$  are neglected due to their negligible effect on phase plate performance [13,18].

Following the method of Ref. [42], the optimization routine satisfies two MTF-based performance requirements to achieve EDoF imaging. First, to improve the performance of each system by increasing through-focus MTF values at specific spatial frequencies, and second to decrease through-focus performance variation by minimizing the MTF value differences for the selected spatial frequencies. The optimization frequencies were selected by identifying the specific frequency ranges exhibiting low values in the through-focus MTF performance of each lens, and directly implemented in the merit function. The selected spatial frequencies for each aspheric lens are summarized in Table 3-1.

Table 3-1: Optimization frequencies used to design EDoF phase plates for the selected aspheric lenses.

Lens NA	Optimization spatial frequencies (cycles/mm)
0.25	60, 86, 124, 240
0.33	61, 98, 115, 270
0.50	80, 160, 320, 480

Three LPPs were designed based on the described criteria, one for each aspheric lens. Table 3-2 summarizes the surface parameters and sags of each design. Figure 3-3 shows 3D plots for the surface of the LPPs designed for the 0.25 and 0.50 NA lenses.

Table 3-2: LPP surface coefficients and sags for lenses with 0.25, 0.33 and 0.50 NA values.

Lens NA	$\alpha$ coefficient	$\beta$ coefficient	Phase plate sag ( $\mu\text{m}$ )
0.25	$5.754 \times 10^{-8}$	1	5.6
0.33	$7.138 \times 10^{-8}$	1	7.1
0.50	$5.794 \times 10^{-7}$	0	40.6

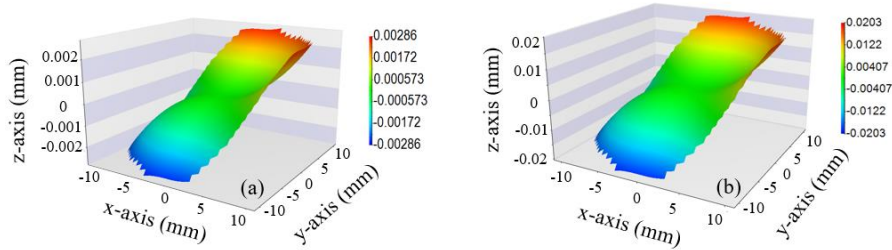


Figure 3-3: 3D surface map for the LPPs designed for (a) 0.25 and (b) 0.50 NA lenses over 22 mm clear aperture.

### 3.3.2 Variable logarithmic phase plate design and results

As discussed above, researchers have previously demonstrated the use of an analytical method to derive the freeform surface equation of a phase plate pair that generates a desired wavefront deformation through relative lateral shifts [27,43]. In this approach, the wavefront deformation is proportional to the derivative of the freeform surface in the phase plate pair and the relative shift amount between the pair. However, this approach cannot solve for wavefront deformations caused by mathematical surface descriptions and derivatives with interdependent terms and parameters. In our case, the composite surface created by the shifted VLPPP includes logarithmic and XY-polynomial interdependent terms that are not conducive to analytic integration. As a consequence, we apply the numerical approach demonstrated in Ref. [43] for the VLPPP design. In this approach, two boundary elements are defined in the form of point clouds, along with the desired relative shift for the phase plate pair, to design variable freeform elements utilizing numerical integration techniques.

For the present work, the boundary elements are the LPPs designed for the 0.25 and 0.50 NA aspheric singlets, and the maximum desired shift between the phase plate pair is set as  $\pm 2$  mm. The relative shift between the phase plate pair components is chosen based

on the required clear aperture, manufacturing constraints, and opto-mechanical requirements. The boundary surface diameters are set by adding at least twice the maximum desired shift amount between the pair to their clear apertures to ensure all rays transmit through the surfaces. For this example, a 26 mm aperture was divided into  $501 \times 501$  sample points. After calculating the required VLPPP surfaces, the relative shift required to enable EDoF for the 0.33 NA lens was calculated by minimizing the difference between the composite surface from the VLPPP as surfaces were incrementally shifted to the LPP designed for 0.33 NA lens. The point clouds representing VLPPP surfaces were then implemented in CODE V as NURBS surfaces, which allow for implementing height maps with unequal spacing as the base optical surface with no need to define conventional surface properties (radius of curvature, conic constant, etc.) [44,45]. The VLPPP surfaces were then shifted to quantify the performance of the system. Figure 3-1(b) shows the schematic of the 0.25 NA aspheric lens with shifted VLPPP as an example. The three fixed LPPs are thus replaced by one VLPPP.

Table 3-3: VLPPP design results.

Lens NA	Relative phase plate shift (mm)	Phase plate sag ( $\mu\text{m}$ )
0.25	-2	35.3
0.33	0.44	
0.50	2	

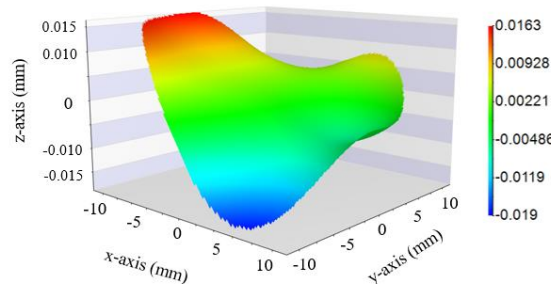


Figure 3-4: 3D surface map of one of the variable logarithmic phase plates over 22 mm clear aperture.

Table 3-3 summarizes the shifts required to enable EDoF for each aspheric lens, and Figure 3-4 shows a 3D plot of one of the VLPPP surfaces.

### 3.4 LPP and VLPPP Performance Analysis

#### 3.4.1 On-axis system performance

This section analyzes the on-axis performance of the LPPs and VLPP by considering both ray and wave-based models.

##### 3.4.1.1 Through-focus spot diagrams

Figure 3-5 qualitatively compares the through-focus spot diagrams for the three lenses with and without the LPP and VLPPP. As expected, the spot sizes increase with the addition of phase plates, with smaller variation over the designed range of focus ( $-6\Delta z$  to  $+6\Delta z$ ). The VLPPP systems create larger spots compared to the LPP designs. More quantitative comparisons are presented below.

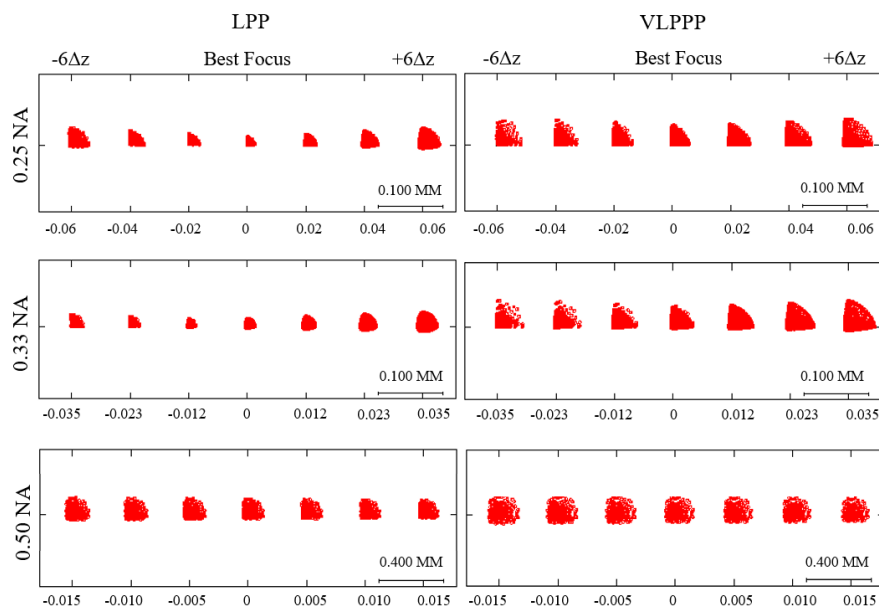


Figure 3-5: Through-focus spot diagrams for 0.25, 0.33, and 0.50 NA lenses with LPP and VLPPP.

### 3.4.1.2 Through-focus MTF

As discussed in Sec. 2, the addition of EDoF phase plates decrease system sensitivity to defocus at the expense of reduced resolution. Figure 3-6 shows the tangential MTF at best focus for all the lenses with and without LPP and VLPPP. With the addition of EDoF phase plates, the on-axis MTF worsens at the best image plane for both phase plates, with LPP performing better than VLPPP, particularly for lower NA lenses.

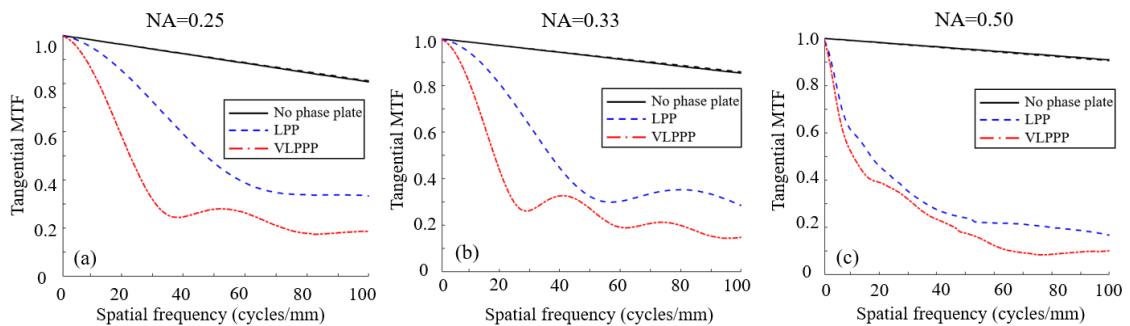


Figure 3-6: Tangential MTF at the best focus for the (a) 0.25, (b) 0.33, and (c) 0.50 NA lenses with and without EDoF phase plates.

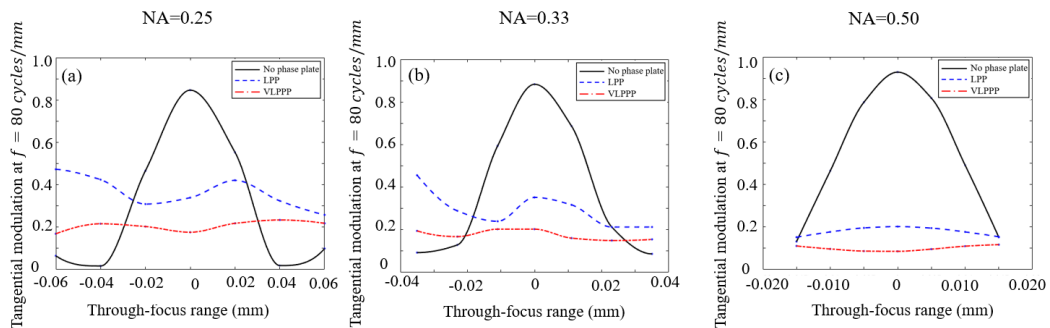


Figure 3-7: On-axis through-focus tangential MTF plots (at  $f = 80$  cycles/mm) for the (a) 0.25, (b) 0.33, and (c) 0.50 NA lenses with and without LPPs and VLPPP.

To illustrate the through-focus on-axis performance of the designed phase plates, Figure 3-7 represents the through-focus tangential modulation values for all the lenses with and

without EDoF phase plates at 80 cycles/mm as an example. The through-focus variation of the MTF decreases with the addition of the phase plates. The peak MTF values are also lower, as expected.

### 3.4.1.3 Root-mean-square (RMS) deviation of PSF and slope of RMS deviation of PSF

To qualitatively analyze the effect of EDoF phase plates on system performance, we consider the through-focus PSF variation by calculating the RMS deviation of PSF and its slope introduced previously [42]. For the RMS deviation of PSF calculation, the normalized PSF at best focus and defocus image planes are used to find the RMS values, following Eq. (3.3):

$$RMS = \sqrt{\frac{1}{m^2} \sum_{i=1}^m \sum_{j=1}^m (PSF_{d,i,j} - PSF_{f,i,j})^2} . \quad (3.3)$$

In Eq. (3.3),  $m^2$  is the total number of samples in the PSF matrix and  $PSF_{d,i,j}$  and  $PSF_{f,i,j}$  are the normalized PSF (in matrix form and  $m=1024$ ) at the defocused and best focus planes, respectively. The slope of RMS deviation of PSF calculation, which represents the rate at which the RMS deviation of PSF changes through focus, is calculated as follows:

$$s_i = \frac{RMS_{i+1} - RMS_i}{d_{i+1} - d_i}, i = 1, 2, \dots, 6, \quad (3.4)$$

where  $RMS_{i+1}$  and  $RMS_i$  are the RMS deviations of PSF values calculated for the image planes at  $d_{i+1}$  and  $d_i$  locations respectively, and  $s_i$  is the slope of the RMS deviation of PSF for each two consecutive defocus image planes. With the addition of EDoF phase plates, smaller RMS values are expected, which confirms less through-focus variation in PSF. As an example, Figure 3-8 shows the normalized PSFs using diffraction-based models for the

0.33 NA lens with its respective shifted VLPPP at best focus and  $\pm 4\Delta z$  image plane locations.

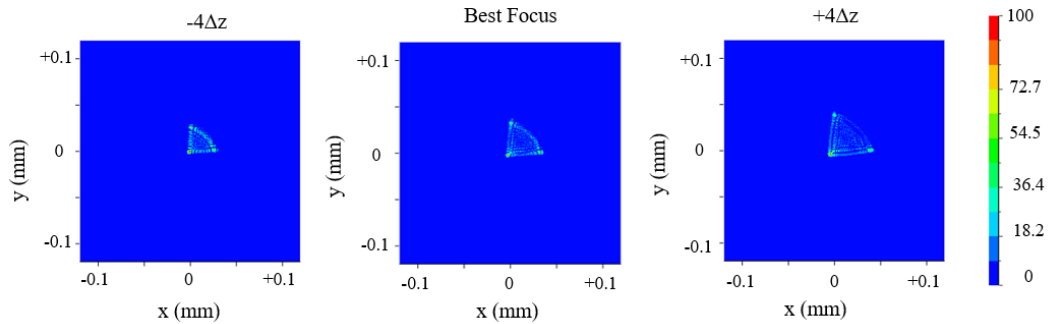


Figure 3-8: Normalized PSFs for the 0.33 NA lens with its respective shifted VLPPP at best focus and  $\pm 4\Delta z$  image plane locations.

Based on literature [13,18], the LPP enables EDoF over a larger defocus range and therefore, the axial ranges over which the RMS deviation of PSFs are calculated are extended to study phase plate performance. Figure 3-9 compares the RMS deviation of PSF and its slope for the three lenses with and without LPP and VLPPP over defocus range of  $-10\Delta z$  to  $+10\Delta z$ . With the addition of LPP and VLPPP, the RMS deviation of PSF shows smaller values and the slope of the RMS deviation of PSF exhibits lower values and through-focus variation, confirming more consistent through-focus performance. Since the addition of VLPPP introduces more surfaces and thickness in the optical system, lower performance is expected compared to the equivalent LPP. This behavior is more pronounced in the lower NA systems. The LPP and its equivalent shifted VLPPP show similar performance for the 0.50 NA lens.

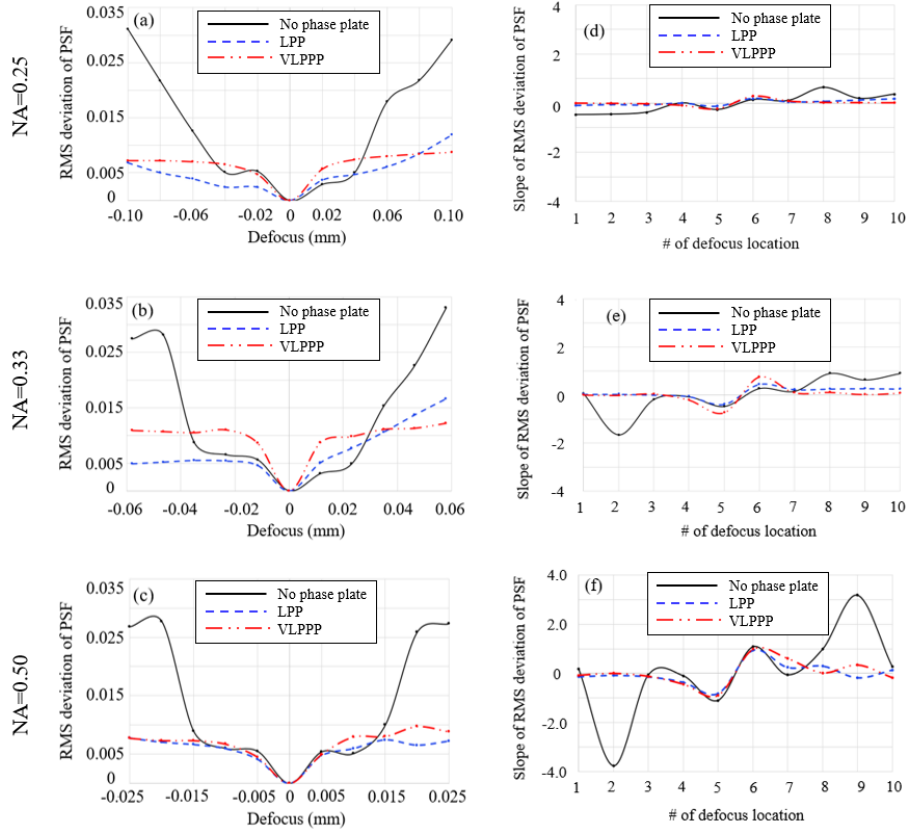


Figure 3-9: RMS deviation of PSF through-focus and its slope for (a,d) 0.25, (b,e) 0.33, and (c,f) 0.50 NA lenses with and without the LPP and VLPPP phase plates.

### 3.4.2 Off-axis system performance

For imaging applications, it is also essential to consider system performance for off-axis object location. This section considers and compares the performance of the designed LPPs and VLPPP over a 3-degree field along the y-axis, as shown in Figure 3-10.

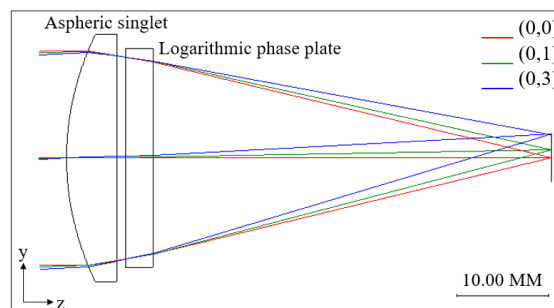


Figure 3-10: Location of field angles along the y-axis.

### 3.4.2.1 Through-focus spot diagrams vs. field angle

We consider the through-focus spot diagrams (ray-based models) for the 0.33 NA lens as an example. As the field angle increases along the y-axis, the spot sizes and shapes for the LPP and VLPPP change (Fig. 3-11). The location of the smallest spot also changes at higher field angles which is expected due to field dependent aberrations. This performance trend is also observed for the 0.25 and 0.50 NA lenses with LPP and VLPPP.

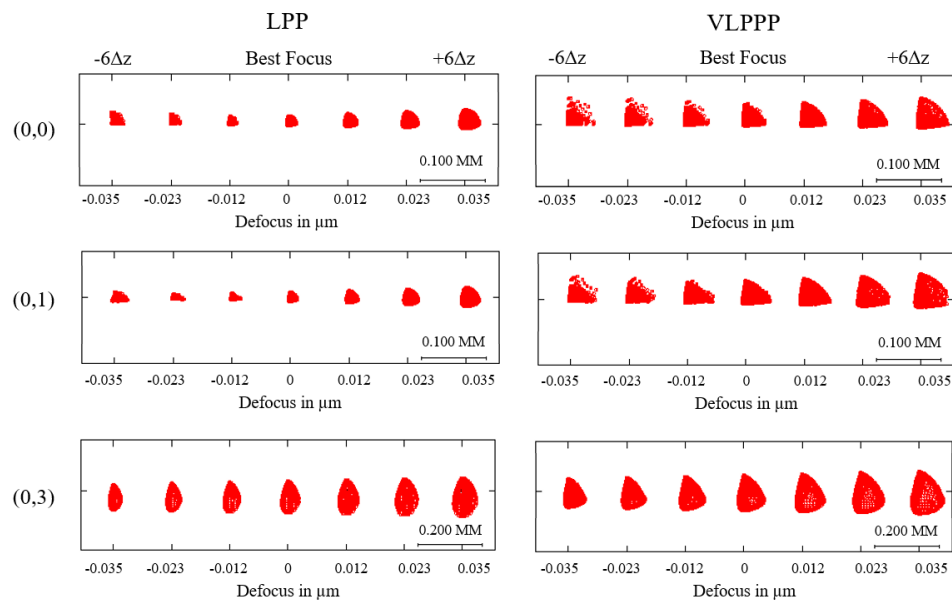


Figure 3-11: Through focus spot diagrams (from  $-6\Delta z$  to  $+6\Delta z$ ) for the 0.33 NA lens with LPP and VLPPP over a 3-degree field angle along the y-axis.

### 3.4.2.2 MTF vs. field angle

As mentioned previously, system performance degrades with an increase in field angle. As an example, we consider tangential MTF plots at best focus for the 0.33 NA lens with and without the EDoF phase plates at the discussed field points (Fig. 3-12). At higher field angles, the MTF value decreases overall, worsening the system's performance. This is expected due to the on-axis nature of the optimization routine discussed in Sec. 2. The

comparison in Figure 3-12 also shows the performance for the 0.33 NA lens with VLPPP at (0,0) and (0,1) degree field points is very similar, with the higher field angle point performing slightly better at some frequencies.

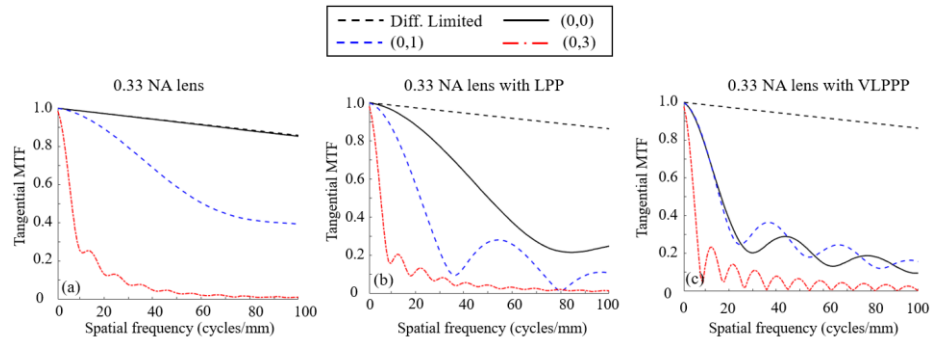


Figure 3-12: MTF at best focus for (a) 0.33 NA lens, (b) 0.33 NA lens with LPP and (c) 0.33 NA lens with VLPPP over a 3-degree field angle along the y-axis.

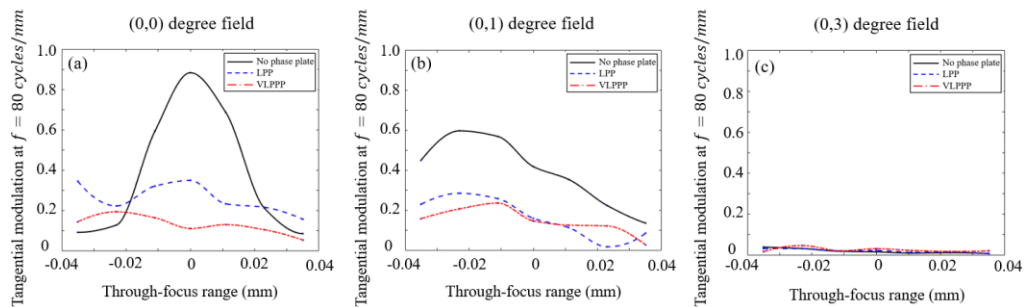


Figure 3-13: Through-focus tangential modulation at  $f = 80$  cycles/mm for 0.33 NA lens with and without EDoF phase plates at (a) (0,0), (b) (0,1), and (c) (0,3) field angles along the y-axis.

Since it is expected to observe less through-focus MTF variation with the addition of EDoF phase plates, we consider the through-focus tangential modulation plots for the 0.33 NA lens with and without EDoF phase plates over the 3-degree field angle in Figure 3-13. As expected, at higher field angles the location of the best image plane changes, resulting in a shift in the maximum modulation value location which becomes less pronounced at

higher field angles due to lower overall performance. However, the addition of phase plates leads to less modulation variation.

### 3.5 LPP and VLPPP Performance Comparison to CPP and QPPP

As discussed previously, LPPs have been reported to enable EDoF in imaging systems over a larger range of defocus compared to CPPs designed for the same imaging systems [13,18]. Therefore, as an example, we compare the through-focus spots and RMS deviation of PSF of the previously designed CPPs and QPPP [42] with the current LPPs and VLPPP over a larger range of defocus ( $\pm 10\Delta z$ ). Figure 3-14 compares the through-focus spot diagrams for the 0.33 NA lens with and without CPP and LPP as an example. With the addition of the EDoF phase plates, the through-focus spots become larger and less sensitive to defocus qualitatively.

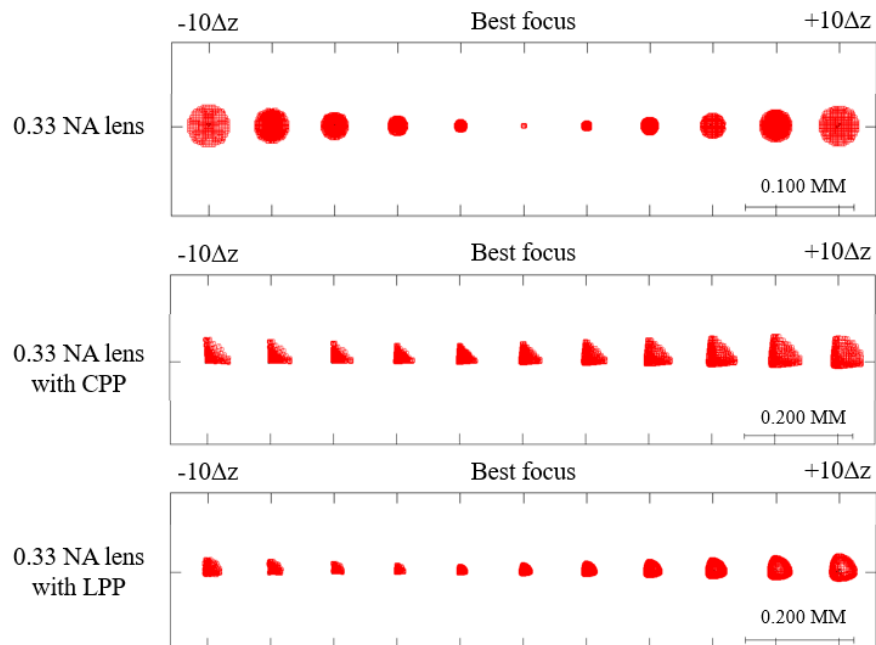


Figure 3-14: Through-focus ( $-10\Delta z$  to  $+10\Delta z$ ) spot diagrams for the 0.33 NA lens with and without the EDoF phase plates.

Figure 3-15 compares the RMS deviation of PSF values for the 0.25, 0.33, and 0.50 NA lenses with and without CPPs, LPPs, QPPP and VLPPP. All phase plates are designed for the same lens and with the same optimization goals, and the only differences are the surface descriptions of the phase plates. For the lower NA lenses (0.25 and 0.33), the CPPs perform similar to or slightly better than the LPPs. For the highest NA lens, the CPP has lower RMS deviation of PSF over the designed range of defocus, suggesting a consistent through-focus performance. However, the LPP RMS values decrease or are closer to the RMS value for the designed CPP for  $|\text{defocus}| > 6\Delta z$ . This suggests that the LPP can enable EDoF for higher NA lenses and over a larger range of defocus compared to CPP. For the VLPPP and QPPP performance comparison, Figure 3-15 shows that the RMS deviation of PSF values are smaller for the QPPP for the lower NA lenses, creating more consistent through-focus spots compared to VLPPP. For the highest NA lens, the QPPP and VLPPP comparison show that over the designed range of defocus, QPPP has a smaller RMS deviation of PSF, and over a larger range defocus range, the VLPPP performs better only on one side of the focus. However, the slope of the RMS deviation of PSF through-focus for the highest NA lens with VLPPP is smaller compared to QPPP. Therefore, for higher NA lenses and over large ranges of defocus, VLPPP could be advantageous due to its ability to create less and/or slow varying PSFs compared to the QPPP.

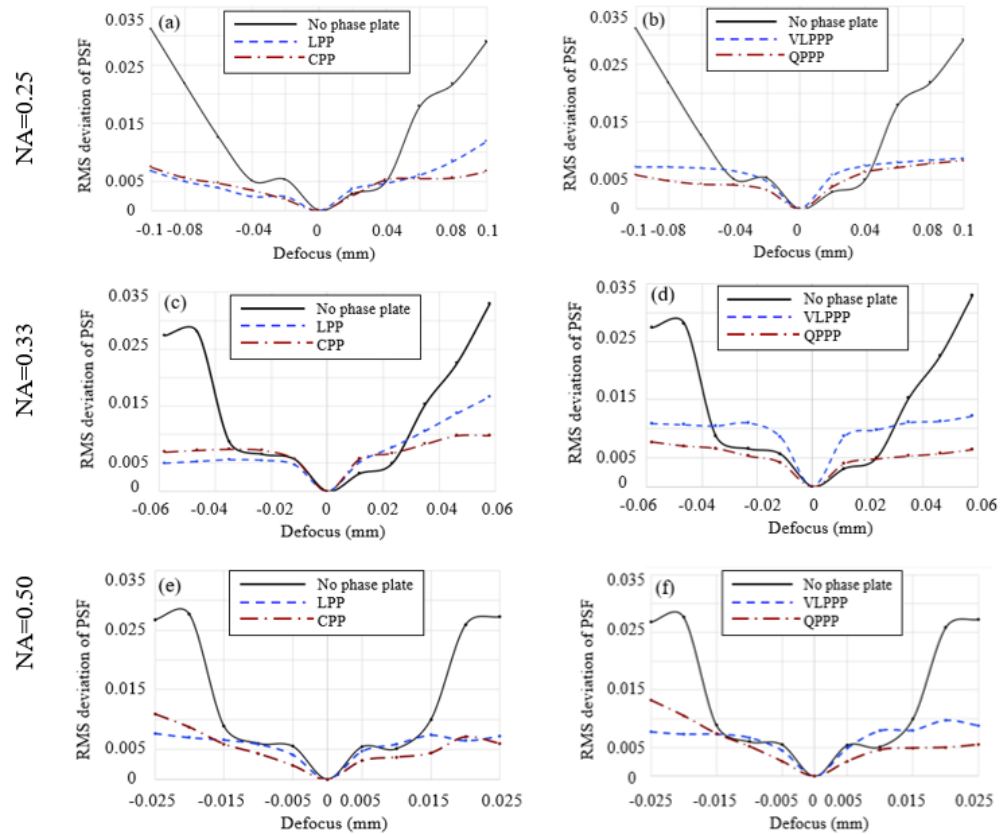


Figure 3-15: Comparison of RMS deviation of PSF and its slope between previously designed CPP and QPPP with current LPP and VLPPP designs for (a,b) 0.25, (c,d) 0.33, and (e,f) 0.50 NA lenses.

### 3.6 Discussion and Conclusion

In this paper, we have proposed a method to design a phase plate pair that enables variable extended depth of field through relative translation of the phase components using a numerical design approach. Three fixed phase plates with logarithmic surface description were designed initially for commercial lenses with different NA values. The motivation for selection of logarithmic surface type was its reported capability to enable EDoF over a larger defocus range compared to the CPPs. The LPP surface parameters were optimized to meet two design goals: (1) improving on-axis system MTF by increasing the MTF values at specific spatial frequencies and (2) decreasing on-axis MTF variation through focus by

minimizing the MTF differences at the selected frequencies. One VLPPP then replaced three LPPs to enable EDoF for the baseline lenses. For the VLPPP design a numerical method was used instead of an analytical approach. The need for use of the numerical approach was rooted in logarithmic and XY-polynomial interdependent terms in the surface description of the LPP. This method leverages numerical integration (developed in MATLAB) to find the required variable surfaces. The implementation of the LPPs required user-defined surfaces and the VLPPP was implemented using NURBS user-defined surfaces in CODE V.

The performance of the designed EDoF phase plates (LPPs and VLPPP) were considered for both ray- and wave-based models and on- and off-axis rays. The through-focus spot diagrams qualitatively showed that with the addition of the LPPs and VLPPP, the on-axis spots become larger and less sensitive to defocus. A similar comparison over the 3-degree field angle (along the y-axis) showed that the spot sizes and shapes vary through field and the location of the smallest spot shifts at higher field angles due to the presence of field-dependent aberrations such as field curvature. These comparisons confirmed that both LPPs and VLPPP enable focus-invariant systems, with their best performance on-axis.

As a quantitative metric, we also compared the RMS deviation of PSF and its slope for the LPPs and VLPPP. These metrics represent the self-similarity of the through-focus PSFs and the rate at which the PSFs change through-focus respectively. As the image plane location moves across the optic axis and away from the nominal best focus in a standard imaging system, the PSF changes and therefore, the RMS deviation of PSF gets larger

through focus. With the addition of the LPPs and VLPPP, the RMS deviation of PSF values and their slope were reduced.

The MTF at best focus and through-focus were also studied for each lens with and without EDoF phase plates (on- and off-axis) which showed that system MTF decreases and varies less through-focus with the addition of the phase plates. These observations were consistent for both on- and off-axis fields, with the systems performing worse off-axis which is expected due to the on-axis nature of the optimization routine. The field sensitivity of the system performance can be linked to the asymmetries in the surfaces of the phase plates and the directionality of the shifts between the VLPPP components. Further analyses could be performed on the 2D MTF of the EDoF phase plates and performance metrics such as the Minimum Modulation Curve [46,47]. In addition, optimization methods that consider the off-axis performance of the phase plates have the potential to improve the imaging quality of these systems.

As mentioned previously, the motivation for this work was the suggestion by the literature that the LPP enables EDoF over a larger range of defocus compared to CPP. As a result, a comparison was performed for the through-focus spots and RMS deviation of PSFs for the previously designed CPPs and QPPP with the current LPPs and VLPPP. Our observations showed that for the lower NA lenses, the LPPs and equivalent VLPPP do not offer a great performance advantage over the CPPs and QPPP. However, for the highest NA lens the performance difference between the CPP and LPP (and the QPPP and VLPPP) is more pronounced and the rate at which the RMS deviation of PSF varies through-focus is smaller. Additional design and optimization are needed to further investigate the LPP and VLPPP performance for lenses with higher NA values.

### 3.7 References

1. T. S. Tkaczyk, "Field Guide to Microscopy," SPIE Field Guides (SPIE press, Bellingham, Washington USA, 2010).
2. M. Bass, E.W. V. Stryland, D. R. Williams, and W. L. Wolfe, "Handbook of Optics Volume II Devices," Measurements, and Properties 2nd edition (1995).
3. E. Dowski and G. Johnson, "Wavefront coding: a modern method of achieving high-performance and/or low-cost imaging systems," SPIE's International Symposium on Optical Science, Engineering, and Instrumentation (SPIE, 1999), Vol. 3779.
4. W. Chi and N. George, "Electronic imaging using a logarithmic asphere," *Opt. Lett.* 26(12), 875–877 (2001).
5. K. Chu, N. George, and W. Chi, "Incoherently combining logarithmic aspheric lenses for extended depth of field," *Appl. Opt.* 48(28), 5371–5379 (2009).
6. Z. Zhai, S. Ding, Q. Lv, X. Wang, and Y. Zhong, "Extended depth of field through an axicon," *J. Mod. Opt.* 56(11), 1304–1308 (2009).
7. F. Zhou, R. Ye, G. Li, H. Zhang, and D. Wang, "Optimized circularly symmetric phase mask to extend the depth of focus," *J. Opt. Soc. Am. A* 26(8), 1889–1895 (2009).
8. R. N. Zahreddine and C. J. Cogswell, "Binary phase modulated partitioned pupils for extended depth of field imaging," in *Imaging and Applied Optics 2015*, OSA Technical Digest (online) (Optical Society of America, 2015), IT4A.2.
9. K. Chu, N. George, and W. Chi, "Extending the depth of field through unbalanced optical path difference," *Appl. Opt.* 47(36), 6895–6903 (2008).
10. J. Ojeda-Castaneda, J. E. A. Landgrave, and H. M. Escamilla, "Annular phase-only mask for high focal depth," *Opt. Lett.* 30(13), 1647–1649 (2005).

11. R. Zahreddine, R. Cormack, and C. Cogswell, "Simultaneous quantitative depth mapping and extended depth of field for 4D microscopy through PSF engineering," in SPIE BiOS, (SPIE, 2012),
12. E. R. Dowski and W. T. Cathey, "Extended depth of field through wave-front coding," *Appl. Opt.* 34(11), 1859–1866 (1995).
13. S. S. Sherif, W. T. Cathey, and E. R. Dowski, "Phase plate to extend the depth of field of incoherent hybrid imaging systems," *Appl. Opt.* 43(13), 2709–2721 (2004).
14. G. Carles, "Analysis of the cubic-phase wavefront-coding function: Physical insight and selection of optimal coding strength," *Opt. Lasers Eng.* 50(10), 1377–1382 (2012).
15. J. van der Gracht, E. R. Dowski, M. G. Taylor, and D. M. Deaver, "Broadband behavior of an optical–digital focus-invariant system," *Opt. Lett.* 21(13), 919–921 (1996).
16. H. Zhao, Q. Li, and H. Feng, "Improved logarithmic phase mask to extend the depth of field of an incoherent imaging system," *Opt. Lett.* 33(11), 1171–1173 (2008).
17. H. Zhao and Y. Li, "Performance of an improved logarithmic phase mask with optimized parameters in a wavefrontcoding system," *Appl. Opt.* 49(2), 229–238 (2010).
18. S. Sherif, E. Dowski, and W. T. Cathey, "Logarithmic phase filter to extend the depth of field of incoherent hybrid imaging systems," in International Symposium on Optical Science and Technology, (SPIE, 2001),
19. S. Prasad, T. Torgersen, V. Pauca, R. Plemmons, and J. van der Gracht, "Engineering the pupil phase to improve image quality," in AeroSense 2003, (SPIE, 2003),

20. S. Bagheri, P. Silveira, R. Narayanswamy, and D. Pucci de Farias, “Design and optimization of the cubic-phase pupil for the extension of the depth of field of task-based imaging systems,” in *SPIE Optics +Photonics*, (SPIE, 2006),
21. L. W. Alvarez, “Two-element variable-power spherical lens,” *U.S.* 3(305), 294 (1967).
22. M. Bawart, A. Jesacher, P. Zelger, S. Bernet, and M. Ritsch-Marte, “Modified Alvarez lens for high-speed focusing,” *Opt. Express* 25(24), 29847–29855 (2017).
23. A. W. Lohmann, “A New Class of Varifocal Lenses,” *Appl. Opt.* 9(7), 1669–1671 (1970).
24. S. Barbero, “The Alvarez and Lohmann refractive lenses revisited,” *Opt. Express* 17(11), 9376–9390 (2009).
25. J. A. Shultz and T. J. Suleski, “Design of a Variable Toric Lens Using Laterally Shifted Freeform Elements,” in *Optical Design and Fabrication 2017 (Freeform, IODC, OFT)*, OSA Technical Digest (online) (Optica Publishing Group, 2017), JW2C.2.
26. M. Bawart, A. Jesacher, S. Bernet, and M. Ritsch-Marte, “Remote focusing in confocal microscopy by means of a modified Alvarez lens,” *J. Microsc.* 271(3), 337–344 (2018).
27. I. A. Palusinski, J. M. Sasián, and J. E. Greivenkamp, “Lateral-shift variable aberration generators,” *Appl. Opt.* 38(1), 86–90 (1999).
28. T. Mitchell and J. Sasian, “Variable aberration correction using axially translating phase plates,” *AeroSense ‘99 (SPIE, 1999)*, Vol. 3705.
29. E. Acosta and S. Bará, “Variable aberration generators using rotated Zernike plates,” *J. Opt. Soc. Am. A* 22(9), 1993–1996 (2005).
30. S. Shadalou, W. J. Cassarly, and T. J. Suleski, “Tunable illumination for LED-based systems using refractive freeform arrays,” *Opt. Express* 29(22), 35755–35764 (2021).

31. T. Suleski, J. Shultz, and P. Smilie, “Dynamic beam shaping with freeform optics,” SPIE Optical Engineering + Applications (SPIE, 2014), Vol. 9194.
32. P. J. Smilie and T. J. Suleski, “Variable-diameter refractive beam shaping with freeform optical surfaces,” *Opt. Lett.* 36(21), 4170–4172 (2011).
33. T. Hellmuth, A. Bich, R. Börret, A. Holschbach, and A. Kelm, “Variable phaseplates for focus invariant optical systems,” in *Optical Systems Design 2005*, (SPIE, 2005),
34. J. Ojeda-Castañeda, E. A. Gomez, H. P. Mora, M. T. Cisneros, E. R. Ledesma Orozco, J. S. Pacheco Santamaria, J. G. Martinez Castro, and R. C. Salas Segoviano, “Optical System With Variable Field Depth,” U.S. 8,159,753 B2 (2012).
35. J. Ojeda-Castañeda and C. M. Gómez-Sarabia, “Tuning field depth at high resolution by pupil engineering,” *Adv. Opt. Photonics* 7(4), 814–880 (2015).
36. J. Ojeda-Castañeda, J. E. A. Landgrave, and C. M. Gómez-Sarabia, “Conjugate phase plate use in analysis of the frequency response of imaging systems designed for extended depth of field,” *Appl. Opt.* 47(22), E99–E105 (2008).
37. A. Castro and J. Ojeda-Castañeda, “Asymmetric phase masks for extended depth of field,” *Appl. Opt.* 43(17), 3474–3479 (2004).
38. L. Ledesma-Carrillo, R. Guzmán-Cabrera, C. M. Gómez-Sarabia, M. Torres-Cisneros, and J. Ojeda-Castañeda, “Tunable field depth: hyperbolic optical masks,” *Appl. Opt.* 56(1), A104–A114 (2017).
39. M. Demenikov, G. Muyo, and A. R. Harvey, “Experimental demonstration of continuously variable optical encoding in a hybrid imaging system,” *Opt. Lett.* 35(12), 2100–2102 (2010).

40. S. S. Rege, T. S. Tkaczyk, and M. R. Descour, “Application of the Alvarez-Humphrey concept to the design of a miniaturized scanning microscope,” *Opt. Express* 12(12), 2574–2588 (2004).
41. “Edmund Optics”, retrieved <https://www.edmundoptics.com/f/precision-aspheric-lenses/13139>.
42. S. Moein and T. J. Suleski, “Freeform optics for variable extended depth of field imaging,” *Opt. Express* 29(24), 40524–40537 (2021).
43. S. Shadalou and T. J. Suleski, “General design method for dynamic freeform optics with variable functionality,” *Opt. Express* 30(11), 19974–19989 (2022).
44. “CODE V Lens System Setup Reference Manual,” (2021).
45. “User-defined features in CODE V,” (2009).
46. H. Aryan, G. D. Boreman, and T. J. Suleski, “The Minimum Modulation Curve as a tool for specifying optical performance: application to surfaces with mid-spatial frequency errors,” *Opt. Express* 27(18), 25551–25559 (2019).
47. G. D. Boreman, “Modulation transfer function in optical and electro-optical systems,” *Tutorial texts in optical engineering (SPIE)*, Vol. TT121.

## CHAPTER 4: FABRICATION AND CHARACTERIZATION OF FREEFORM OPTICS FOR VARIABLE EXTENDED DEPTH OF FIELD IMAGING

### 4.1 Abstract

Point spread function engineering uses specially designed phase plates placed at the exit pupil of an imaging system to reduce sensitivity to defocus. A custom phase plate is typically required for each system to enable extended depth of field imaging, so methods enabling variable extended depth of field imaging are of particular interest. This article discusses the fabrication of previously designed extended depth of field fixed phase plates with cubic and variable phase plate pairs with quartic surface profiles, as well as the qualitative and quantitative performance characterization of these plates using a point source microscope. Experimental results are compared with predicted performance from simulation and demonstrate that the fixed and variable phase plates perform as intended in enabling EDoF, with experimental performance being slightly lower than predicted performance.

### 4.2 Introduction

Depth of field (DoF), which is defined as the region in object space over which imaging systems can create a sharp image, decreases as the numerical aperture (NA) of the system increases [1, 2]. Methods that enable Extended Depth of Field (EDoF) for improved image quality are of particular interest. Point Spread Function (PSF) engineering is a technique that uses a special optical component at the exit pupil to enable EDoF in imaging systems by modifying the PSF of the system to reduce its sensitivity to defocus at the expense of image quality. A high-quality image is then retrieved using computational methods [3, 4].

A broad range of phase plates with varying surface profiles have been used to engineer the PSF to enable EDoF imaging. Logarithmic aspheres[5, 6] , axicons [7, 8], and binary and annular phase modulated components [9-12] are some examples with rotationally symmetric profiles, and the cubic [4, 13-15] and logarithmic [16-19] surfaces are examples of asymmetric (freeform) EDoF phase plates. These phase plates are designed specifically for each optical system. As a result, techniques enabling tunable EDoF are desirable, potentially reducing the number of component and cost. Researchers have previously reported phase plate pairs that enable tunable EDoF by adjusting the relative location of the phase components. Phase plate pairs with polynomial, sinusoidal, or Gaussian surfaces are examples that benefit from phase element lateral translation or rotation to produce a variable EDoF effect [20-25].

We have previously reported on the design of freeform phase plates with variable EDoF for lenses with varying NA values [21]. The design incorporated Cubic Phase Plates (CPP) as a baseline [4, 26]. Then, a Quartic Phase Plate Pair (QPPP) was then designed using an analytical approach [27] to enable EDoF for the range of lenses via relative translation of the phase plates along the x-axis. The freeform surface profiles of the of the CPP and QPPP are given by Eqs. (4.1) and (4.2), respectively:

$$z(x, y) = \alpha(x^3 + y^3), \quad (4.1)$$

$$z(x, y) = \beta\left(\frac{x^4}{4} + xy^3\right), \quad (4.2)$$

where  $\alpha$  and  $\beta$  are surface coefficients. Figure 4-1 [21] illustrates the concept around which the variable EDoF phase pair is based. Multiple fixed phase plates can be replaced with a single pair of shifted phase plates to enable EDoF for lenses with different NA values.

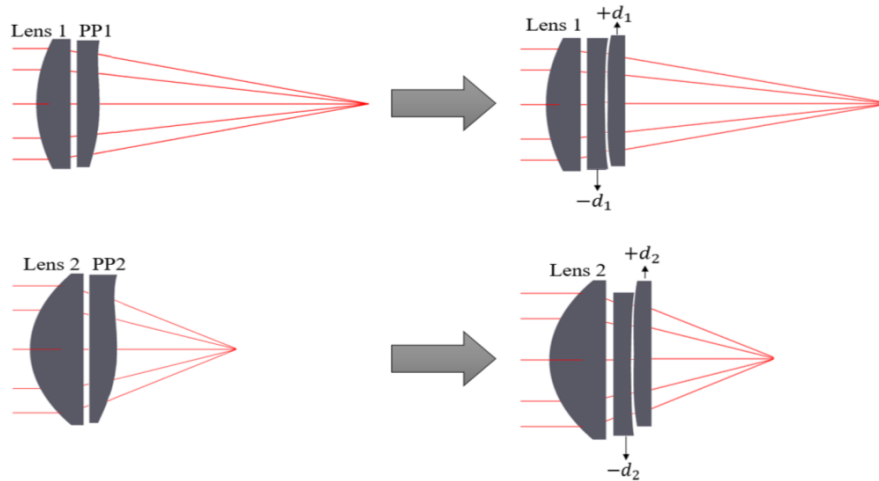


Figure 4-1: Two fixed Phase Plates (PP1 and PP2) are replaced with one freeform phase plate pair to enable EDoF through the relative translation of the phase plates along the x-axis [21].

In this paper we report on fabrication and experimental characterization method and results for the CPP and QPPP designs from [21]. The surface parameters for the CPPs and QPPP are summarized in Tables 4-1 and 4-2.

Table 4-1: Cubic phase plate optimization results.

Lens NA	$\Delta z$ ( $\mu\text{m}$ )	Optimized $\alpha$	Phase plate sag ( $\mu\text{m}$ )
0.25	10.1	$2.473 \times 10^{-6}$	8.6
0.33	5.8	$6.317 \times 10^{-6}$	21.9
0.5	2.5	$1.804 \times 10^{-5}$	62.4

Table 4-2: Quartic phase plate pair design results.

Lens NA	$\Delta z$ ( $\mu\text{m}$ )	Relative phase plate shift (mm)	Phase plate sag ( $\mu\text{m}$ )
0.25	10.1	0.269	90
0.33	5.8	0.700	
0.5	2.5	2.000	

Since these freeform EDoF phase plates lack rotational symmetry, manufacturing processes require more degrees of freedom than those used in conventional optics. Advances in ultra-precision machining have enabled fabrication of freeform surfaces by allowing different machine geometries [28]. We discuss the design and fabrication of custom optomechanical fixturing, as well as the freeform EDoF phase plates.

Researchers have previously evaluated EDoF phase plate performance by imaging a point source, spoke target, or other objects at different axial locations (defocus) [23, 29-34]. In this paper, we demonstrate a novel use of a Point-Source Microscope (PSM) to characterize the performance of the designed phase plates [35]. The PSM can be thought of as a modern autostigmatic microscope [36], and can be used for a variety of purposes, including optical alignment and centration [37, 38], wavefront quality measurement [39], and radius of curvature measurement [40]. For our work, the PSM is used in confocal mode to capture the through-focus spots for imaging lenses with and without EDoF phase plates. The measured spots are then analyzed to quantify the through-focus spot variation and enable experimental performance comparisons between the different systems.

## 4.3 Optical and Optomechanical Fabrication

### *4.3.1 Optical system architecture*

As discussed above, freeform optical systems with variable functionality typically rely on relative translational motion between the freeform surfaces from flexures or precision translational mounts. To expedite manufacturing and allow for more stable alignment and testing, we chose instead to fabricate the freeform surfaces for the QPPP with pre-set shifts on the surfaces corresponding to the desired lens NA under test, as shown in Figure 4-2.

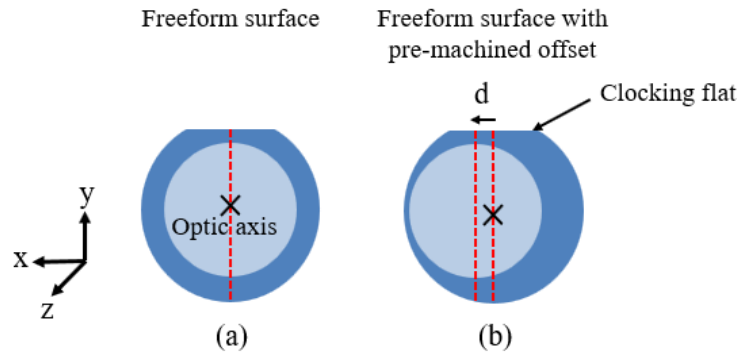


Figure 4-2: Simplified image of (a) freeform surface and (b) the QPPP surface, shifted in the x-direction by distance  $d$ .

The resulting optical system architecture (Fig. 4-3) consists of two optical component mounts, one for the aspheric lens and one for the CPP (or QPPP), two steel alignment pins, six magnets (three for each mount) and the optical components.

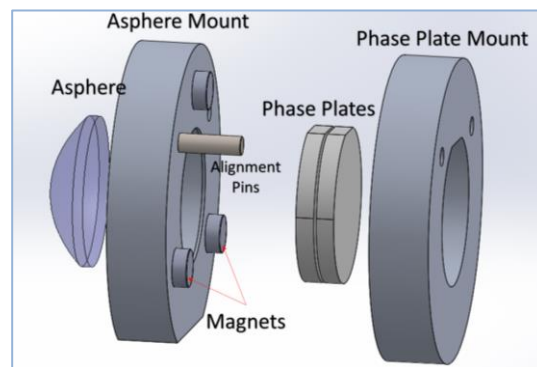


Figure 4-3: Exploded view of CAD model for quartic phase plate test system.

#### 4.3.2 Manufacturing of optomechanical fixturing

Optical testing of the freeform phase plates requires a mounting system that encourages modularity. For this optomechanical design, housings were made for each of the aspheric lenses, CPPs, and QPPPs. The housings were all machined from the same piece of turned

aluminum bar stock with 63.5 mm outer diameter to facilitate tolerance and alignment preservation. The requirement of specialty manufactured optomechanical housings came from the tight tolerances within the optical system design. Among all the optical systems (CPPs and QPPP), the smallest spacing tolerance was  $\pm 50 \mu\text{m}$ . Each mount was then machined on the HAAS Computer Numerically Controlled (CNC) Toolroom mill (Fig. 4-4).

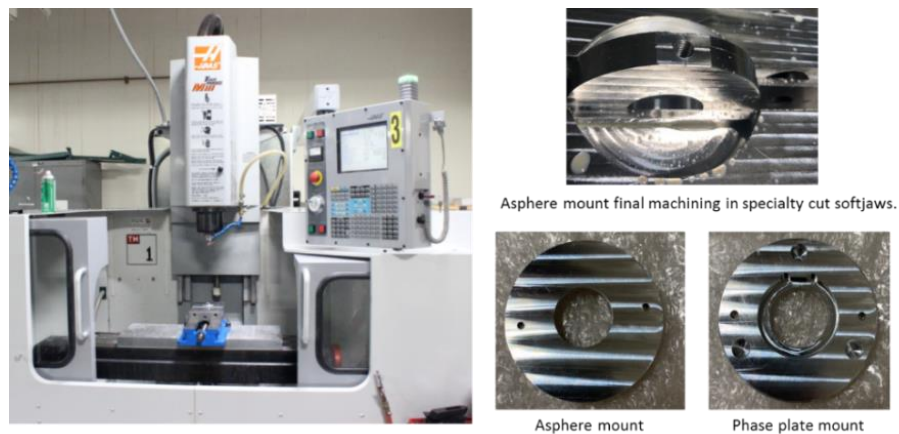


Figure 4-4: A HAAS CNC Toolroom Mill with manufactured mountings.

For the asphere mounts, each lens with different numerical aperture (NA) was held in place by a slip ring. The air gap between the asphere and phase plate was required to be no greater than 1 mm. This tightly controlled distance was split between the asphere mount back face and the phase plate front face. Hardened steel machine pins with an outer diameter of 3.175 mm and neodymium magnets were used to clock and hold the housings together for testing. Magnets were used instead of fasteners (such as threaded rods or bolts) to avoid over-constraining the system and to enable modularity in the testing set-ups. For the phase plate mounts, the CPP tests required only the one optic, so all the CPP mounts were thinner than the QPPP mounts.

### 4.3.3 Optical fabrication

Two main limiting factors of freeform optical manufacturing are requirements for precision control and final surface finish. Freeform surface manufacturing requires at least three axes of motion [41]. For the freeforms in our system, this geometry is enabled through a precision manufacturing diamond turning lathe and coordinated multi-axis machining, aka Slow Tool Servo (STS). STS is a lathe-based machining method that leverages three separate axes (X, Z, C). As the diamond tool feeds across the rotating surface in the X direction, the machine synchronizes the angular location of the part (C axis) with the distance of the tool in the Z direction, relative to the part's translational and angular position. Coordinated axis diamond turning typically leaves 2 – 15 nm RMS surface roughness, depending on the material, while enabling complex freeform surface manufacture [42, 43].

For toolpath surface generation, NanoCAM4® (a precision manufacturing software package) was leveraged. NanoCAM4® allows for the direct import of the freeform surface equations to form a manufacturing toolpath, As shown above in Figure 4-2 and Table 4-2, the optical datum within NanoCAM4® was offset by the required distance along the x-axis for each QPPP and the machining toolpath was processed and exported for usage.

Manufacturing of the freeform phase plates were completed in two phases: (1) Rough shaping of optical blanks, and (2) Ultraprecision coordinated-axis diamond turning of the freeform optical surfaces. Rough machining methods are useful for quickly removing large amounts of material with moderate precision, while diamond turning is used for precision shaping capabilities and the fact that optical material can be turned to a specular finish with virtually no tool wear [44].

Initial blanking began with 31.75 mm round bar stock PMMA rough-cut on a horizontal band saw into approximately 5 mm thick disks. Both sides of these disks were then ‘faced’ (cut smooth) with a 1.008 diamond tool with 1.008 mm nose radius on the Moore Nanotech 350FG using a 38.1 mm diameter aluminum vacuum chuck. The Moore Nanotech 350FG (Fig. 4-5), is a 5-axis precision diamond machining center with 3 linear axes (X, Y, Z) with 0.034 nm resolution and two rotary axes (B, C) with 1.75 nanoradian resolution. Total manufacturing volume on this machine is 350 mm by 150 mm by 300 mm (X, Y, Z). The machine is enclosed in a temperature-controlled room at 20 C +/- 0.1 degrees C at 50% relative humidity to minimize thermal variations during manufacturing.

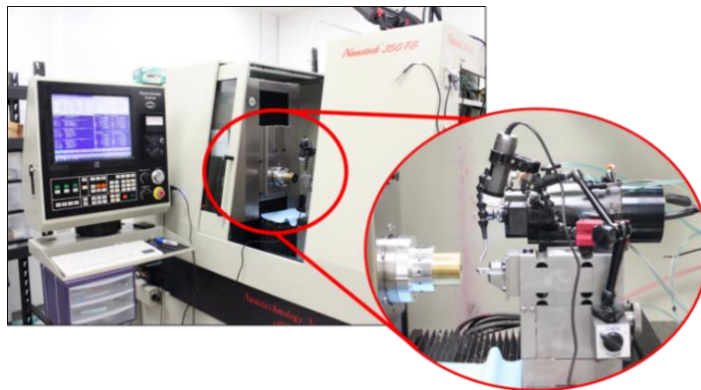


Figure 4-5: Moore Nanotech 350FG 5-axis ultraprecision diamond machining system at UNC Charlotte.

Once the rough-cut blanks were faced on the front and back sides, the parts were milled on a HAAS Toolroom Mill (Fig. 4-4) to cut clocking flats for angular alignment of the parts. A clocking flat guillotine was made using the HAAS mill and two steel pins pressed into two drilled and reamed holes in a machined aluminum block. The Outer Diameters (OD) of the steel machine pins aligned with a circumscribed circle which matched with the optic’s OD. This design allowed for an endmill with a known diameter to cut off a flat on

the optic blank's outer diameter. The optical blanks were next taken back to the Moore Nanotech 350FG for final machining. Both faces of the optical blanks were machined to the desired thickness with parallelism of  $\pm 1 \mu\text{m}$ . To generalize, these optical surfaces are comprised of a raised outer ring, ranging from 5 to 100  $\mu\text{m}$  raised above the freeform clear aperture, as shown in Figure 4-6. The main function of the outer ring is to help set the air gap between the QPPP components.

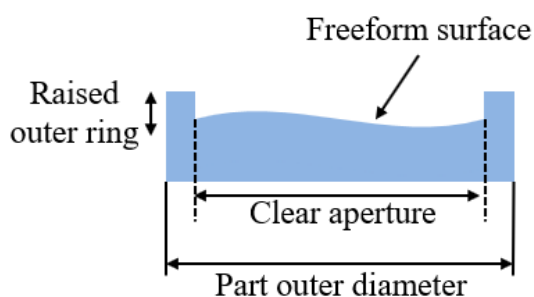


Figure 4-6: Schematic of the phase plates with the machined raised outer ring.

The final diamond machining of the freeform CPP and QPPP optical surfaces specified in Eqs. (4.1) and (4.2) and Tables 4-1 and 4-2 were completed on the Moore 350FG using the NanoCAM4® generated toolpaths. Both CPPs and QPPs required up to four rough STS cutting passes at a Depth of Cut (DOC) of 20  $\mu\text{m}$  with a stepover of 15  $\mu\text{m}$ , and an angular density of 1 degree. These rough cutting passes were followed with single precision finishing pass with 15  $\mu\text{m}$  DOC 5  $\mu\text{m}$  stepover, and an angular density of 0.4 degrees. The optics were mounted for final surface cutting used a 10 PSI vacuum and a layout fluid. (Layout fluid is a thin liquid, useful for mounting small parts on a vacuum chuck. When it dries, the layout fluid can act as a thin adhesive with no adverse effects on PMMA, unlike some other glues).

We were unable to measure the form of the resulting freeform optics at this time, but from prior experience we expect the form accuracy on the Moore Nanotech 350FG to be better than 0.5  $\mu\text{m}$  Peak-to-Valley (PV) [45]. Surface finish was measured using the Zygo Zegage™ Plus 3D optical surface profiler (Fig. 4-7). The optical surfaces were measured using 20x and 50x objectives with 3 averages and a Gaussian bandpass filter of 2.5 to 80  $\mu\text{m}$ , following ISO 10110-8 [46]. These filters were chosen to isolate surface roughness from form or waviness. The average root mean squared (RMS) surface roughness across the phase plates is 11 nm.

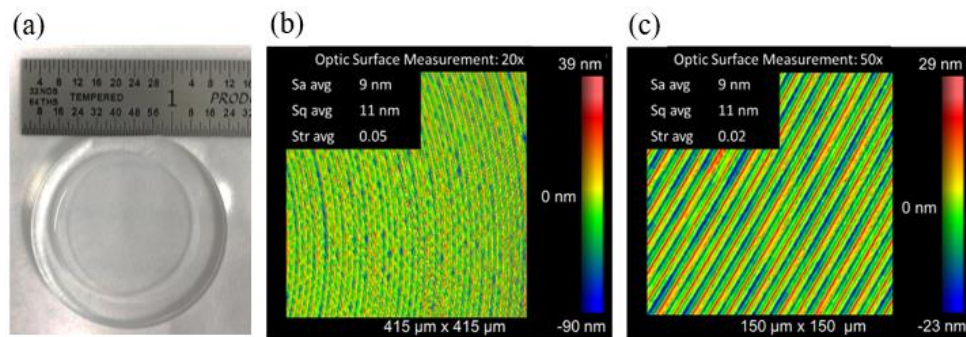


Figure 4-7: (a) Image of a finished QPP, and interferometric measurement of a finished QPPP using the Zygo Zegage™ Plus 3D optical surface profiler and the average surface roughness measurements for the (b) 20x and (c) 50x objectives.

#### 4.4 Performance Characterization Method, Results and Analysis

##### 4.4.1 Autostigmatic and point source microscopes

PSM can be thought of as a modern realization of an Autostigmatic Microscope (ASM) [36]. In an ASM, a point source of light is imaged perfectly by a microscope objective after being reflected off a beam splitter. The focused light is then re-imaged at the eyepiece,

forming a perfect image. This configuration is illustrated in Figure 4-8, modeled after Ref. [36].

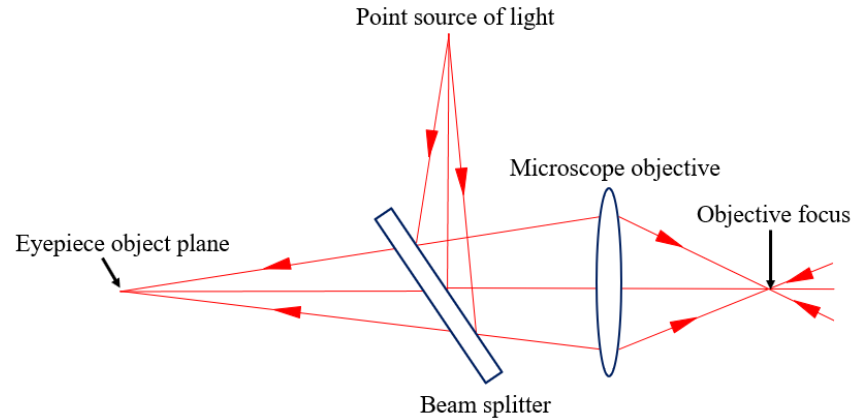


Figure 4-8: Simple Autostigmatic Microscope configuration.

ASM can be used in a variety of applications, including measurement and alignment. For example, the radius of curvature of a convex mirror can be found by first positioning the focus of ASM objective at the center of curvature of the spherical surface (confocal reflection), and then moving the ASM to focus on the surface of the sphere (cat's eye reflection). The distance between the two focus spots is the radius of the spherical surface, as shown in Figure 4-9 [36].

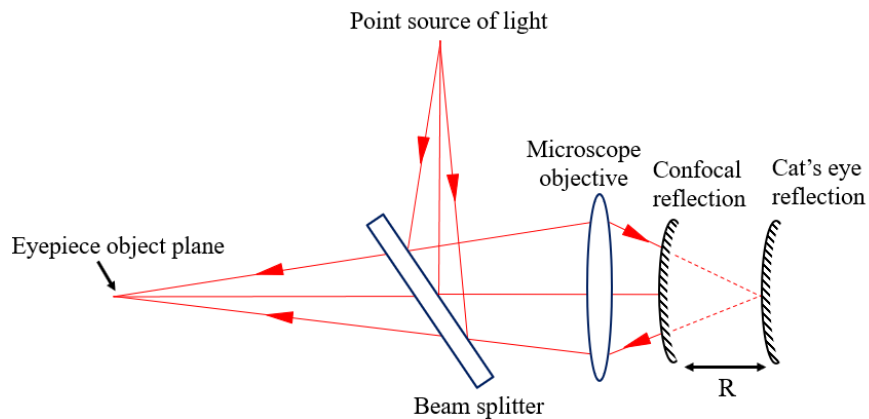


Figure 4-9: Measuring radius of curvature of a spherical reflective surface using ASM.

The PSM operates in the same way as an ASM, except that it has two light paths. In the PSM, a point source (fiber coupled laser diode at 635 nm) is accompanied with a Kohler light source (LEDs) to create a powerful reflected light imaging microscope. The addition of the Kohler light source enables imaging of opaque surfaces and uniform illumination of the sample under test. Figure 4-10 shows the schematic of a PSM [36].

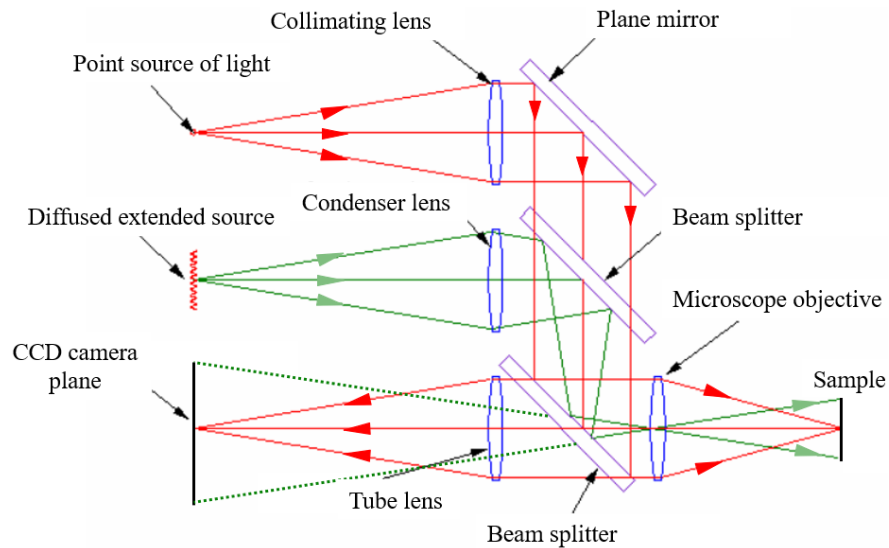


Figure 4-10: Schematic of a PSM, with illumination and imaging paths [36].

#### 4.4.2 Use of PSM to characterize through-focus performance

We consider the use of PSM in the configuration shown in Figure 4-11 (a) to characterize the through-focus performance of the EDoF phase plates. To the best of our knowledge, the PSM has not been previously used to measure through-focus spots or to investigate the effects of EDoF phase plates on PSF variation. The PSM enables the creation of a point-like source and, when displaced along the optic axis, enables measurement of the PSF through focus. The microscope objective and the imaging system under test have their foci aligned in a confocal configuration. The imaging system (lens

and phase plates) is displaced along the optic axis using a translation stage with micrometer and the spot variation is measured to perform a focus scan and characterize the imaging system's performance.

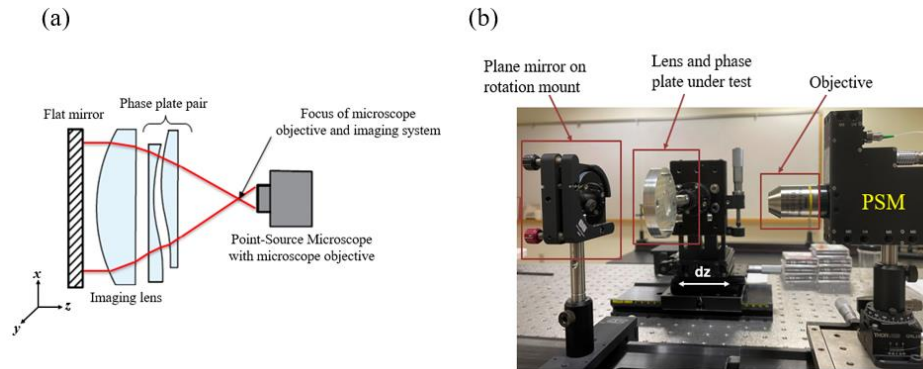


Figure 4-11: (a) Schematic of experimental setup (top view) for characterization of variable EDoF imaging, and (b) experimental setup (side view) for phase plate characterization.

It is anticipated that the addition of EDoF phase plates (CPPs and QPPPs) will result in larger through-focus spots with less variation than would be observed in the absence of phase plates. Figure 4-11 (b) shows the experimental setup. Translation and rotation stages are used in the experimental setup for both through-focus scanning and alignment. The NA of the microscope objective and imaging system under test are matched for the measurement.

#### 4.4.3 Performance characterization

##### 4.4.3.1 Through-focus spot measurements

For the purpose of this study, we consider the through-focus spot measurements for the 0.33 NA lens with and without EDoF phase plates. The theoretical through-focus range of

interest for this lens is from  $-34.8 \mu\text{m}$  to  $+34.8 \mu\text{m}$  ( $-6\Delta z$  to  $+6\Delta z$ ), where  $\Delta z$  is calculated using Eq. (4.3) [2] :

$$\Delta z = \frac{n\lambda}{NA^2}, \quad (4.3)$$

where  $n$  is the refractive index of the surrounding medium ( $n = 1$  for air),  $\lambda = 633 \text{ nm}$  (design wavelength), and  $NA = 0.33$  (lens numerical aperture). Due to the micrometer resolution of  $1 \mu\text{m}$ , the experimental defocus scan range is from  $-36 \mu\text{m}$  to  $+36 \mu\text{m}$ , in  $6 \mu\text{m}$  steps. Figure 4-12 shows the PSM measurements of through-focus spot for the 0.33 NA lens with and without the corresponding CPP and QPPP elements (Tables 4-1 and 4-2). As discussed previously, the QPPP elements are manufactured with  $0.7 \text{ mm}$  shift in opposite directions to enable EDoF, which eliminates misalignment errors caused by additional degree of freedom required for phase plate pair translation.

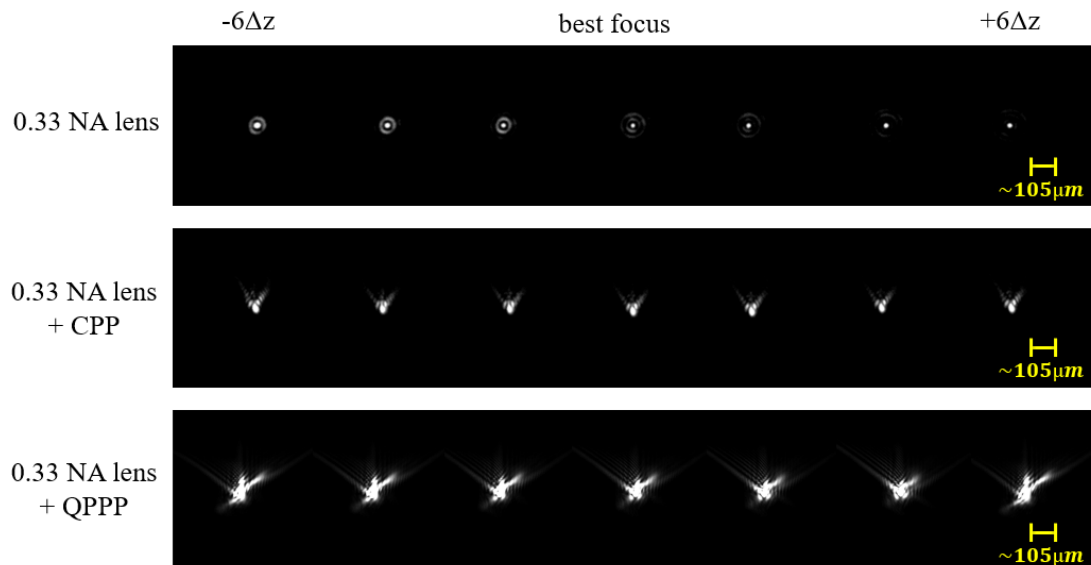


Figure 4-12: Through-focus spot measurements from  $-36 \mu\text{m}$  to  $+36 \mu\text{m}$  ( $-6\Delta z$  to  $+6\Delta z$ ), for the 0.33 NA lens with and without EDoF phase plates.

As expected, qualitative examination of Figure 4-12 shows observable through-focus spot variation for the aspheric lens with no phase plate. With the addition of CPP and QPPP, larger spots are created with less variation as the lens is displaced along the optic axis and moved away from the optimum best focus. We present quantitative analyses of these observations in the next section.

#### 4.4.3.2 Root-Mean-Square (RMS) deviation of spots

For a qualitative performance comparison of the EDoF phase plates, we introduce the Root-Mean-Square (RMS) of the normalized spots through focus [21]. To calculate this parameter, the through-focus spot intensity measurement matrices ( $I$ ) are first normalized in MATLAB, using the “*rescale*” command, which scales a data array to the interval of interest [ $a$   $b$ ]. Each intensity matrix is rescaled using the equation below:

$$I_{norm} = a + [(I - I_{min}) ./ (I_{max} - I_{min})] .* (b - a), \quad (4.4)$$

where  $a$  and  $b$  are the lower and upper boundaries that the array is to be normalized to (0 and 1 in our calculations),  $I$  is the data array to be normalized, and  $I_{min}$  and  $I_{max}$  are the minimum and maximum values of the input array  $I$  [47]. After the intensity measurements for all through-focus and optimum focus locations are normalized, the RMS deviation of the normalized intensities are calculated, using Eq. (4.4):

$$RMS = \sqrt{\frac{1}{m^2} \sum_{i=1}^m \sum_{j=1}^m (I_{norm_{d,i,j}} - I_{norm_{f,i,j}})^2}, \quad (4.5)$$

where  $m$  is the number of elements in the intensity matrix  $I$  (after cropping the data to desired size), and  $I_{norm,d,i,j}$  and  $I_{norm,f,i,j}$  are the normalized image intensities (in matrix form) at defocus and optimum best focus image planes. Figure 4-13 shows the RMS deviation of the spots for the 0.33 NA lens with and without CPP and QPPP. It is evident that the RMS deviation values becomes smaller overall with the addition of the phase plates. However, the CPP spots and RMS deviation are smaller than for the QPPP. As noted in Ref. [21], the CPPs are designed to meet specific through-focus performance requirements, whereas the QPPPs are designed from on CPPs and are not optimized further. The air gap between the QPPP components also contributes to lower QPPP performance.

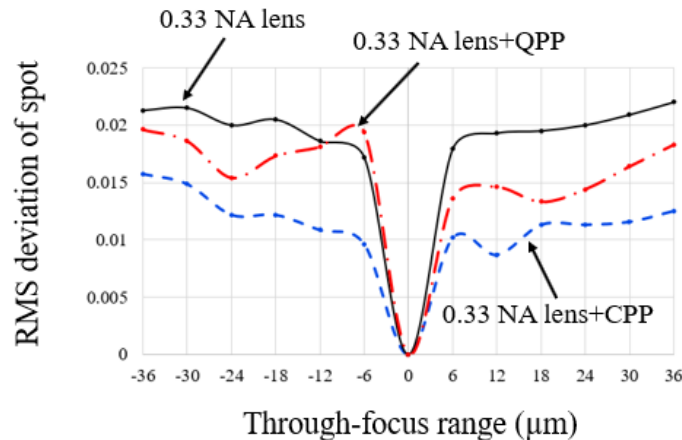


Figure 4-13: Experimental RMS deviation of normalized spots from  $-36\ \mu\text{m}$  to  $+36\ \mu\text{m}$  ( $-6\Delta z$  to  $+6\Delta z$ ), for the 0.33 NA lens with and without EDoF phase plates.

Figure 4-14 compares the normalized PSF and spot measurement at best focus and optimum focus for the 0.33 NA lens with and without CPP and QPPP. We note that the simulation shows diffraction limited performance and PSF for the case of the 0.33 NA lens with no phase plate, while the experiment shows a larger spot. This difference could be

attributed to the differences in simulation and test system layouts, shown in Figures 4-1 and 4-11(a), respectively. In simulations, the wavefront passes through the lens once, whereas in the experimental setup, the wavefront passes through the same lens twice. This difference results in additional spherical aberration and a larger spot.

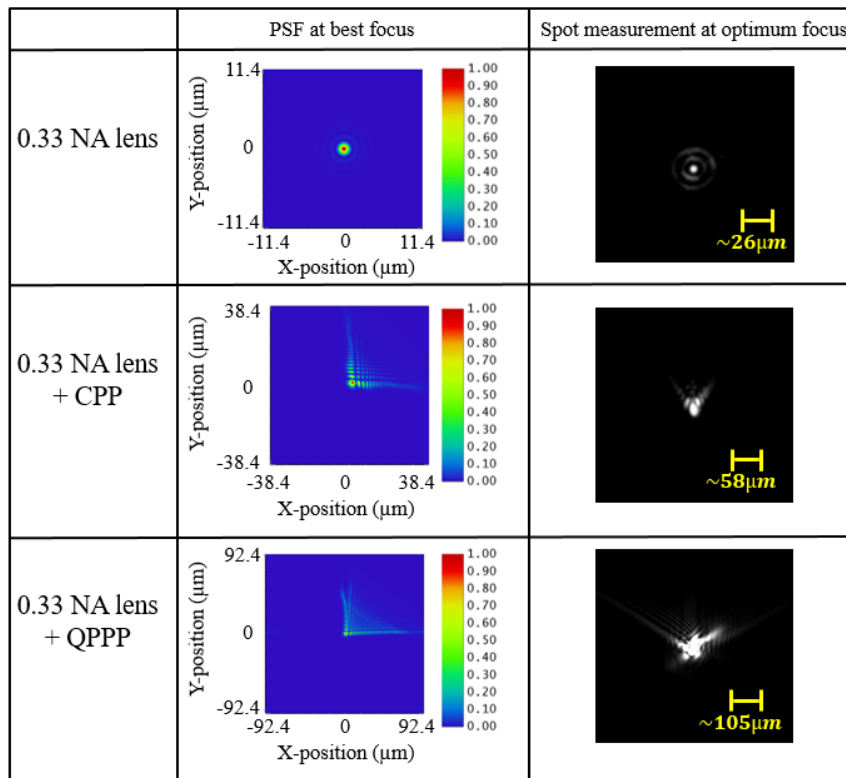


Figure 4-14: Simulated PSF at best focus and measured spot at optimum focus for the 0.33 NA lens with and without EDoF phase plates.

We observe a rotation in the measured spot compared to the simulated PSF for the 0.33 NA lens with the CPP, which is caused by the CPP's orientation along the optic axis with respect to the aspheric lens (about 45 degrees clocking), as well as a change in the shape of the spot. The shape of the measured spot is similar to that of a family of beams with cubic wavefronts and Seidel coma aberration [48]. We observe a similar rotation of the

spot for the 0.33 NA lens when using the QPPP, as well as a difference in the shape of the measured spot. Further investigation of the manufactured form and quantification of misalignment errors may aid in gaining a better understanding of the shapes of the measured spots.

Figure 4-15 compares the RMS deviation of normalized spots to the previously simulated PSFs [21]. This comparison demonstrates reasonable agreement between the simulated and experimental results, and shows smaller through-focus variation for the CPP and shifted QPPP than the lens alone, with QPPP resulting in larger RMS deviation compared to CPP. However, the RMS deviation of the experimental spot measurements have larger values compared to the simulation data. This difference could be due to the difference in simulation layout and experimental set up, as well as potential misalignments present in the system.

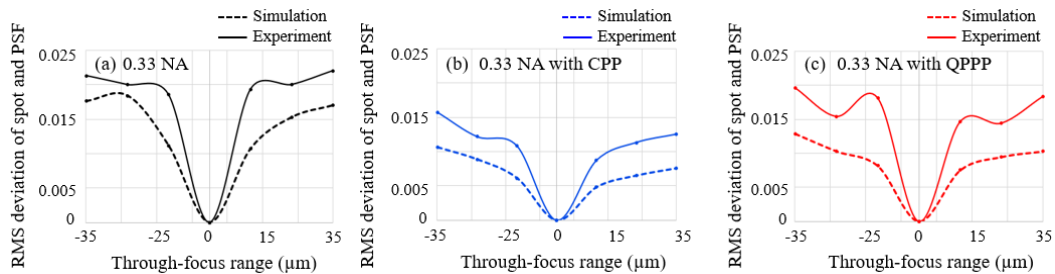


Figure 4-15: Comparison between the RMS deviation of normalized PSF (simulation) and spots (experimental) from  $-36 \mu\text{m}$  to  $+36 \mu\text{m}$  ( $-6\Delta z$  to  $+6\Delta z$ ), for (a) 0.33 NA lens, (b) 0.33 NA lens with CPP and (c) 0.33 NA lens with QPPP.

#### 4.5 Discussion and Conclusion

We have reported on the manufacturing and characterization of an optical system based on previously designed EDoF freeform phase plates [21]. Custom optomechanical

fixturing was designed and fabricated. The freeform surface profiles of the optical phase plates were manufactured using ultraprecision coordinated axis diamond turning, with measured average RMS surface roughness of 11 nm. We demonstrated a novel use of a Point Source Microscope to experimentally measure the through-focus spots of the optical components under test. We note that the configuration in which the PSM was used to determine the spot variation through focus is slightly different from the original layout used for optical design of the freeform phase plates. However, the results show that the PSM can provide useful information about the through-focus performance.

The results of the measurements confirm that the through-focus spots are more consistent with the addition of the EDoF phase plates, but that the addition of phase plates produces larger spots than in the absence of phase plates. This can be determined qualitatively by visually comparing the through-focus spots, and qualitatively by comparing the RMS deviation of the normalized spots. We note that the measured spots at optimal best focus do not perfectly match predictions from software, and that the spots for the 0.33 NA lens with CPP exhibit characteristics of cubic wavefronts (Airy beams) and Seidel comatic beams [48]. Measuring the form error of the manufactured CPPs and quantifying the misalignments in the test setup may provide a better understanding of the reason for the spot shape.

#### 4.6 References

1. M. Bass, E. W. V. Stryland, D. R. Williams, and W. L. Wolfe, *Handbook of Optics Volume II Devices, Measurements, and Properties 2nd edition* (1995).

2. T. S. Tkaczyk, *Field Guide to Microscopy*, SPIE Field Guides (SPIE press, Bellimngham, Washington USA, 2010).
3. S. Bradburn, W. T. Cathey, and E. R. Dowski, "Realizations of focus invariance in optical–digital systems with wave-front coding," *Appl. Opt.* **36**, 9157-9166 (1997).
4. E. R. Dowski and W. T. Cathey, "Extended depth of field through wave-front coding," *Appl. Opt.* **34**, 1859-1866 (1995).
5. W. Chi and N. George, "Electronic imaging using a logarithmic asphere," *Opt. Lett.* **26**, 875-877 (2001).
6. K. Chu, N. George, and W. Chi, "Incoherently combining logarithmic aspheric lenses for extended depth of field," *Appl. Opt.* **48**, 5371-5379 (2009).
7. K. B. Rajesh, Z. Jaroszewicz, and P. M. Anbarasan, "Improvement of lens axicon's performance for longitudinally polarized beam generation by adding a dedicated phase transmittance," *Opt. Express* **18**, 26799-26805 (2010).
8. Z. Zhai, S. Ding, Q. Lv, X. Wang, and Y. Zhong, "Extended depth of field through an axicon," *Journal of Modern Optics* **56**, 1304-1308 (2009).
9. R. N. Zahreddine and C. J. Cogswell, "Binary phase modulated partitioned pupils for extended depth of field imaging," in *Imaging and Applied Optics 2015*, OSA Technical Digest (online) (Optical Society of America, 2015), IT4A.2.
10. J. Ojeda-Castaneda, J. E. A. Landgrave, and H. M. Escamilla, "Annular phase-only mask for high focal depth," *Opt. Lett.* **30**, 1647-1649 (2005).
11. K. Chu, N. George, and W. Chi, "Extending the depth of field through unbalanced optical path difference," *Appl. Opt.* **47**, 6895-6903 (2008).

12. C. J. R. Sheppard, "Binary phase filters with a maximally-flat response," *Opt. Lett.* **36**, 1386-1388 (2011).
13. S. Bagheri, P. E. X. Silveira, and D. P. de Farias, "Analytical optimal solution of the extension of the depth of field using cubic-phase wavefront coding. Part I. Reduced-complexity approximate representation of the modulation transfer function," *J. Opt. Soc. Am. A* **25**, 1051-1063 (2008).
14. S. Prasad, V. P. Pauca, R. Plemmons, T. Torgersen, and J. van der Gracht, *Pupil-phase optimization for extended-focus, aberration-corrected imaging systems*, Optical Science and Technology, the SPIE 49th Annual Meeting (SPIE, 2004), Vol. 5559.
15. S. Prasad, T. Torgersen, V. Pauca, R. Plemmons, and J. van der Gracht, "Engineering the pupil phase to improve image quality," in *AeroSense 2003*, (SPIE, 2003),
16. S. Sherif, E. Dowski, and W. T. Cathey, "Logarithmic phase filter to extend the depth of field of incoherent hybrid imaging systems," in *International Symposium on Optical Science and Technology*, (SPIE, 2001),
17. S. S. Sherif, W. T. Cathey, and E. R. Dowski, "Phase plate to extend the depth of field of incoherent hybrid imaging systems," *Appl. Opt.* **43**, 2709-2721 (2004).
18. H. Zhao, Q. Li, and H. Feng, "Improved logarithmic phase mask to extend the depth of field of an incoherent imaging system," *Opt. Lett.* **33**, 1171-1173 (2008).
19. H. Zhao and Y. Li, "Performance of an improved logarithmic phase mask with optimized parameters in a wavefront-coding system," *Appl. Opt.* **49**, 229-238 (2010).
20. T. Hellmuth, A. Bich, R. Börret, A. Holschbach, and A. Kelm, "Variable phaseplates for focus invariant optical systems," in *Optical Systems Design 2005*, (SPIE, 2005),

21. S. Moein and T. J. Suleski, "Freeform optics for variable extended depth of field imaging," *Opt. Express* **29**, 40524-40537 (2021).
22. J. Ojeda-Castañeda, J. E. A. Landgrave, and C. M. Gómez-Sarabia, "Conjugate phase plate use in analysis of the frequency response of imaging systems designed for extended depth of field," *Appl. Opt.* **47**, E99-E105 (2008).
23. M. Demenikov, G. Muyo, and A. R. Harvey, "Experimental demonstration of continuously variable optical encoding in a hybrid imaging system," *Opt. Lett.* **35**, 2100-2102 (2010).
24. Cristina M. Gómez-Sarabia and J. Ojeda-Castañeda, "Tunable Optical Masks for extended Depth of Field," in *Frontiers in Optics/Laser Science*, (OSA, 2015),
25. Jorge Ojeda-Castaneda, Emmanuel Yépez-Vidal, Eloy García-Almanza, and C. M. Gómez-Sarabia, "Tunable Gaussian mask for extending the depth of field," *PHOTONICS LETTERS OF POLAND* **4**, 115-117 (2012).
26. G. Carles, "Analysis of the cubic-phase wavefront-coding function: Physical insight and selection of optimal coding strength," *Optics and Lasers in Engineering* **50**, 1377-1382 (2012).
27. I. A. Palusinski, J. M. Sasián, and J. E. Greivenkamp, "Lateral-shift variable aberration generators," *Appl. Opt.* **38**, 86-90 (1999).
28. J. P. Rolland, M. A. Davies, T. J. Suleski, C. Evans, A. Bauer, J. C. Lambropoulos, and K. Falaggis, "Freeform optics for imaging," *Optica* **8**, 161-176 (2021).
29. M. Somayaji, V. R. Bhakta, and M. P. Christensen, "Experimental evidence of the theoretical spatial frequency response of cubic phase mask wavefront coding imaging systems," *Opt. Express* **20**, 1878-1895 (2012).

30. M. Demenikov and A. R. Harvey, "Image artifacts in hybrid imaging systems with a cubic phase mask," *Opt. Express* **18**, 8207-8212 (2010).
31. G. Muyo, A. Singh, M. Andersson, D. Huckridge, A. Wood, and A. R. Harvey, "Infrared imaging with a wavefront-coded singlet lens," *Opt. Express* **17**, 21118-21123 (2009).
32. R. N. Zahreddine, R. H. Cormack, and C. J. Cogswell, "Noise removal in extended depth of field microscope images through nonlinear signal processing," *Appl. Opt.* **52**, D1-D11 (2013).
33. R. N. Zahreddine and C. J. Cogswell, "Total variation regularized deconvolution for extended depth of field microscopy," *Appl. Opt.* **54**, 2244-2254 (2015).
34. G. Muyo, A. Harvey, and A. Singh, "High-performance thermal imaging with a singlet and pupil plane encoding," in *European Symposium on Optics and Photonics for Defence and Security*, (SPIE, 2005),
35. "POINT SOURCE MICROSCOPE", retrieved <https://optiper.com/en/products/item/point-source-microscope>.
36. R. Parks, "Versatile autostigmatic microscope," in *SPIE Optics + Photonics*, (SPIE, 2006).
37. R. E. Parks and W. P. Kuhn, "Aligning optical systems containing aspheres with the PSM," in *Frontiers in Optics*, OSA Technical Digest Series (Optica Publishing Group, 2005), FTuE5.
38. E. Milby and J. Burge, "Centration of optical elements," in *SPIE Optical Engineering + Applications*, (SPIE, 2011).

39. W. Kuhn, "A simple tool for alignment and wavefront testing," in *Optical Engineering + Applications*, (SPIE, 2007),
40. R. E. Parks, "A CONTEMPORARY VERSION OF THE AUTOSTIGMATIC MICROSCOPE AND ITS USES" (2016), retrieved <https://optiper.com/en/about/a-contemporary-version-of-the-autostigmatic-microscope-and-its-uses>.
41. K. P. Thompson and J. P. Rolland, "Freeform Optical Surfaces: A Revolution in Imaging Optical Design," *Opt. Photon. News* **23**, 30-35 (2012).
42. K. Abou-El-Hossein, O. Olufayo, and Z. Mkoko, "Diamond tool wear during ultra-high precision machining of rapidly solidified aluminium RSA 905," *Wear* **302**, 1105-1112 (2013).
43. J. Taylor, C. Syn, T. Saito, and R. Donaldson, "Surface Finish Measurements Of Diamond-Turned Electroless-Nickel-Plated Mirrors," *Optical Engineering* **25**, 251013 (1986).
44. C. Bodlapati, T. Dow, A. Wong, and K. Garrard, "Surface finish and diamond tool wear when machining PMMA and PC optics," in *SPIE Optical Engineering + Applications*, (SPIE, 2018),
45. Internal discussion with Prof. Matthew Davies at UNC Charlotte.
46. I. O. f. Standarization, "Optics and photonics — Preparation of drawings for optical elements and systems," in *Surface texture*, (2019).
47. "Rescale", retrieved <https://www.mathworks.com/help/matlab/ref/rescale.html>.
48. S. Vo, K. Fuerschbach, K. P. Thompson, M. A. Alonso, and J. P. Rolland, "Airy beams: a geometric optics perspective," *J. Opt. Soc. Am. A* **27**, 2574-2582 (2010).

## CHAPTER 5: CONCLUSION

### 5.1 Summary

The design and characterization of optical systems that enable tunable EDoF through relative translation of pairs of freeform optical components for lenses with varying NA values have been presented in this dissertation.

In Chapter 2, a phase plate pair with a fourth-order XY-polynomial surface profile was designed that enables variable EDoF for three commercial lenses with varying NA values [94, 96]. This approach considered the design and optimization of fixed phase plates with cubic surface profiles as a baseline. The optimization method leveraged direct implementation of MTF as the optimization metric in the merit function and aimed at improving the on-axis system performance while keeping the performance consistent through-focus and at specific spatial frequencies. An analytical approach was then used to design variable phase plate pair [80]. The results demonstrated that fixed phase plates can be used as a baseline to design one pair of shifted phase plates to enable variable EDoF. The optimization approach also showed that through-focus MTF values (at the design frequencies) can be used as an effective performance metric. However, system MTF and the EDoF performance degraded with the additional of higher field angles.

Chapter 3 featured a phase plate pair with logarithmic surface profiles based on earlier reports of enabling EDoF over a wider defocus range than cubic phase plates [[95]. The design approach and optimization processes were similar to those described in Chapter 2. Multiple fixed phase plates with logarithmic surfaces were designed using the developed MTF-based optimization approach discussed in Chapter 2. A novel numerical approach

was then used to obtain the required surfaces for the variable phase plate pair designs [93]. The results confirmed that the MTF-based optimization approach is applicable to surfaces with varying mathematical descriptions and that the numerical design approach for dynamic freeform surfaces is a powerful tool for calculating the required surfaces for variable EDoF. The off-axis performance of the designs in this chapter were similar to the designs in Chapter 2.

Comparing the results from Chapters 2 and 3 showed that fixed and variable logarithmic-based phase plates do not outperform CPPs and QPPs for lower NA lenses. However, as the lens NA increases, fixed and variable logarithmic phase plates can provide more consistent through-focus performance over a wider range of defocus. Additionally, logarithmic phase plates have smaller surface sags, which may be advantageous for manufacturing and optomechanical assembly.

Chapter 4 discussed optical and optomechanical component manufacturing, and experimental characterization of the fixed and variable phase plates described in Chapter 2. A Point Source Microscope (PSM) was used as a novel method to experimentally characterize the through-focus performance of the 0.33 NA lens. The experimental results showed that both fixed and variable phase plates exhibit focus-invariant behavior throughout their intended axial range of operation.

## 5.2 Future work

1. Investigate and develop optimization techniques that explicitly incorporate performance considerations for wider fields of view.

2. Due to inherent asymmetries in phase plates and optical systems, the 2D modulation transfer function (MTF) may provide further insight into their performance [97, 98]. Additional on and off-axis performance analysis of phase plates utilizing 2D MTF may be beneficial.
3. Investigate the design and characterization of EDoF fixed and variable phase plates for lenses with larger numerical apertures than those considered in this study. As the NA of the lens increases, the system depth of field decreases and enabling EDoF becomes more difficult. As a consequence, it may be necessary to consider additional mathematical descriptions of variable phase plate pair surfaces.
4. Conduct surface tolerance studies on fixed and variable phase plates to determine the effects of surface form errors and mid-spatial frequency errors from manufacturing on optical performance.
5. Image processing/computational imaging to quantify the impacts and capabilities of the fixed and variable phase plat

## REFERENCES:

1. R. Parks, "Versatile autostigmatic microscope," in *SPIE Optics + Photonics*, (SPIE, 2006).
2. M. Bass, E. W. V. Stryland, D. R. Williams, and W. L. Wolfe, *Handbook of Optics Volume II Devices, Measurements, and Properties 2nd edition* (1995).
3. T. S. Tkaczyk, *Field Guide to Microscopy*, SPIE Field Guides (SPIE press, Bellmingham, Washington USA, 2010).
4. M. Minsky, "Microscopy Apparatus," 3,013,467 (1961).
5. M. Gu, C. J. R. Sheppard, and X. Gan, "Image formation in a fiber-optical confocal scanning microscope," *J. Opt. Soc. Am. A* **8**, 1755-1761 (1991).
6. S. W. Paddock, "Principles and practices of laser scanning confocal microscopy," *Molecular Biotechnology* **16**, 127-149 (2000).
7. S. W. Paddock, "Confocal Laser Scanning Microscopy," *BioTechniques* **27**, 992-1004 (1999).
8. S. Murali, K. P. Thompson, and J. P. Rolland, "Three-dimensional adaptive microscopy using embedded liquid lens," *Opt. Lett.* **34**, 145-147 (2009).
9. S. Liu and H. Hua, "Time-multiplexed dual-focal plane head-mounted display with a liquid lens," *Opt. Lett.* **34**, 1642-1644 (2009).
10. W. J. Shain, N. A. Vickers, B. B. Goldberg, T. Bifano, and J. Mertz, "Extended depth-of-field microscopy with a high-speed deformable mirror," *Opt. Lett.* **42**, 995-998 (2017).

11. B. F. Grewe, F. F. Voigt, M. van 't Hoff, and F. Helmchen, "Fast two-layer two-photon imaging of neuronal cell populations using an electrically tunable lens," *Biomed. Opt. Express* **2**, 2035-2046 (2011).
12. S.-H. Lu and H. Hua, "Imaging properties of extended depth of field microscopy through single-shot focus scanning," *Opt. Express* **23**, 10714-10731 (2015).
13. J. Ojeda-Castaneda, R. Ramos, and A. Noyola-Isgleas, "High focal depth by apodization and digital restoration," *Appl. Opt.* **27**, 2583-2586 (1988).
14. E. R. Dowski and W. T. Cathey, "Extended depth of field through wave-front coding," *Appl. Opt.* **34**, 1859-1866 (1995).
15. E. Dowski and G. Johnson, *Wavefront coding: a modern method of achieving high-performance and/or low-cost imaging systems*, SPIE's International Symposium on Optical Science, Engineering, and Instrumentation (SPIE, 1999), Vol. 3779.
16. W. T. Cathey and E. R. Dowski, "New paradigm for imaging systems," *Appl. Opt.* **41**, 6080-6092 (2002).
17. S. Bagheri, P. E. X. Silveira, and G. Barbastathis, "Signal-to-noise-ratio limit to the depth-of-field extension for imaging systems with an arbitrary pupil function," *J. Opt. Soc. Am. A* **26**, 895-908 (2009).
18. R. J. Pieper and A. Korpel, "Image processing for extended depth of field," *Appl. Opt.* **22**, 1449-1453 (1983).
19. H. Wach and E. Dowski, "Noise modeling for design and simulation of computational imaging systems," in *Defense and Security*, (SPIE, 2004),
20. K. Kubala, E. Dowski, and W. T. Cathey, "Reducing complexity in computational imaging systems," *Opt. Express* **11**, 2102-2108 (2003).

21. W. T. Welford, "Use of Annular Apertures to Increase Focal Depth," *J. Opt. Soc. Am.* **50**, 749-753 (1960).
22. M. Mino and Y. Okano, "Improvement in the OTF of a Defocused Optical System Through the Use of Shaded Apertures," *Appl. Opt.* **10**, 2219-2225 (1971).
23. J. Ojeda-Castañeda, L. R. Berriel-Valdos, and E. Montes, "Bessel annular apodizers: imaging characteristics," *Appl. Opt.* **26**, 2770-2772 (1987).
24. J. Ojeda-Castañeda, L. R. Berriel-Valdos, and E. L. Montes, "Line-spread function relatively insensitive to defocus," *Opt Lett* **8**, 458-460 (1983).
25. J. Ojeda-Castañeda, L. R. Berriel-Valdos, and E. Montes, "Spatial filter for increasing the depth of focus," *Opt. Lett.* **10**, 520-522 (1985).
26. W. Chi and N. George, "Electronic imaging using a logarithmic asphere," *Opt. Lett.* **26**, 875-877 (2001).
27. K. Chu, N. George, and W. Chi, "Incoherently combining logarithmic aspheric lenses for extended depth of field," *Appl. Opt.* **48**, 5371-5379 (2009).
28. F. Zhou, R. Ye, G. Li, H. Zhang, and D. Wang, "Optimized circularly symmetric phase mask to extend the depth of focus," *J. Opt. Soc. Am. A* **26**, 1889-1895 (2009).
29. K. B. Rajesh, Z. Jaroszewicz, and P. M. Anbarasan, "Improvement of lens axicon's performance for longitudinally polarized beam generation by adding a dedicated phase transmittance," *Opt. Express* **18**, 26799-26805 (2010).
30. Z. Zhai, S. Ding, Q. Lv, X. Wang, and Y. Zhong, "Extended depth of field through an axicon," *Journal of Modern Optics* **56**, 1304-1308 (2009).
31. R. N. Zahreddine and C. J. Cogswell, "Total variation regularized deconvolution for extended depth of field microscopy," *Appl. Opt.* **54**, 2244-2254 (2015).

32. R. N. Zahreddine and C. J. Cogswell, "Binary phase modulated partitioned pupils for extended depth of field imaging," in *Imaging and Applied Optics 2015*, OSA Technical Digest (online) (Optical Society of America, 2015), IT4A.2.
33. J. Ojeda-Castaneda, J. E. A. Landgrave, and H. M. Escamilla, "Annular phase-only mask for high focal depth," *Opt. Lett.* **30**, 1647-1649 (2005).
34. K. Chu, N. George, and W. Chi, "Extending the depth of field through unbalanced optical path difference," *Appl. Opt.* **47**, 6895-6903 (2008).
35. L. Liu, F. Diaz, L. Wang, B. Loiseaux, J.-P. Huignard, C. J. R. Sheppard, and N. Chen, "Superresolution along extended depth of focus with binary-phase filters for the Gaussian beam," *J. Opt. Soc. Am. A* **25**, 2095-2101 (2008).
36. C. J. R. Sheppard, "Binary phase filters with a maximally-flat response," *Opt. Lett.* **36**, 1386-1388 (2011).
37. S. Abrahamsson, S. Usawa, and M. Gustafsson, "A new approach to extended focus for high-speed high-resolution biological microscopy," in *SPIE BiOS*, (SPIE, 2006),
38. R. Zahreddine, R. Cormack, and C. Cogswell, "Simultaneous quantitative depth mapping and extended depth of field for 4D microscopy through PSF engineering," in *SPIE BiOS*, (SPIE, 2012),
39. G. Carles, "Analysis of the cubic-phase wavefront-coding function: Physical insight and selection of optimal coding strength," *Optics and Lasers in Engineering* **50**, 1377-1382 (2012).
40. S. Prasad, T. Torgersen, V. Pauca, R. Plemmons, and J. van der Gracht, "Engineering the pupil phase to improve image quality," in *AeroSense 2003*, (SPIE, 2003),

41. S. Bagheri, P. Silveira, R. Narayanswamy, and D. Pucci de Farias, "Design and optimization of the cubic-phase pupil for the extension of the depth of field of task-based imaging systems," in *SPIE Optics + Photonics*, (SPIE, 2006),
42. X. Zhang, X. Zhang, G. Shi, J. Zhang, and F. He, *Design and image restoration research of a cubic-phase-plate system*, 5th International Symposium on Advanced Optical Manufacturing and Testing Technologies (SPIE, 2010), Vol. 7655.
43. M. Liu, L. Dong, Y. Zhao, M. Hui, and W. Jia, "Stationary phase analysis of generalized cubic phase mask wavefront coding," *Optics Communications* **298-299**, 67-74 (2013).
44. M. Demenikov and A. R. Harvey, "Image artifacts in hybrid imaging systems with a cubic phase mask," *Opt. Express* **18**, 8207-8212 (2010).
45. G. Muyo, A. Singh, M. Andersson, D. Huckridge, A. Wood, and A. R. Harvey, "Infrared imaging with a wavefront-coded singlet lens," *Opt. Express* **17**, 21118-21123 (2009).
46. M. Somayaji, V. R. Bhakta, and M. P. Christensen, "Experimental evidence of the theoretical spatial frequency response of cubic phase mask wavefront coding imaging systems," *Opt. Express* **20**, 1878-1895 (2012).
47. M. Somayaji and M. P. Christensen, "Enhancing form factor and light collection of multiplex imaging systems by using a cubic phase mask," *Appl. Opt.* **45**, 2911-2923 (2006).
48. J. van der Gracht, E. R. Dowski, M. G. Taylor, and D. M. Deaver, "Broadband behavior of an optical–digital focus-invariant system," *Opt. Lett.* **21**, 919-921 (1996).

49. S. Sherif, E. Dowski, and W. T. Cathey, "Logarithmic phase filter to extend the depth of field of incoherent hybrid imaging systems," in *International Symposium on Optical Science and Technology*, (SPIE, 2001),
50. S. S. Sherif, W. T. Cathey, and E. R. Dowski, "Phase plate to extend the depth of field of incoherent hybrid imaging systems," *Appl. Opt.* **43**, 2709-2721 (2004).
51. H. Zhao, Q. Li, and H. Feng, "Improved logarithmic phase mask to extend the depth of field of an incoherent imaging system," *Opt. Lett.* **33**, 1171-1173 (2008).
52. H. Zhao and Y. Li, "Performance of an improved logarithmic phase mask with optimized parameters in a wavefront-coding system," *Appl. Opt.* **49**, 229-238 (2010).
53. F. Z. Fang, X. D. Zhang, A. Weckenmann, G. X. Zhang, and C. Evans, "Manufacturing and measurement of freeform optics," *CIRP Annals* **62**, 823-846 (2013).
54. Z. Gao, Q. Yuan, X. Li, L. Chen, and J. Ye, "Review of optical freeform surface representation technique and its application," *Optical Engineering* **56**(2017).
55. J. P. Rolland, M. A. Davies, T. J. Suleski, C. Evans, A. Bauer, J. C. Lambropoulos, and K. Falaggis, "Freeform optics for imaging," *Optica* **8**, 161-176 (2021).
56. K. Fuerschbach, J. P. Rolland, and K. P. Thompson, "A new family of optical systems employing  $\phi$ -polynomial surfaces," *Opt. Express* **19**, 21919-21928 (2011).
57. T. Nakano and Y. Tamagawa, "Configuration of an off-axis three-mirror system focused on compactness and brightness," *Appl. Opt.* **44**, 776-783 (2005).
58. A. Bauer, M. Pesch, J. Muschaweck, F. Leupelt, and J. P. Rolland, "All-reflective electronic viewfinder enabled by freeform optics," *Opt. Express* **27**, 30597-30605 (2019).

59. A. Bauer and J. P. Rolland, "Design of a freeform electronic viewfinder coupled to aberration fields of freeform optics," *Opt. Express* **23**, 28141-28153 (2015).
60. J. Ye, J. Yu, Z. Song, S. Pei, Q. Yuan, Z. Gao, and Y. He, "Design of a compact off-axis two-mirror freeform infrared imager with a wide field of view," *Journal of Modern Optics* **66**, 304-311 (2019).
61. D. Michaelis, S. Kudaev, R. Steinkopf, A. Gebhardt, P. Schreiber, and A. Bräuer, *Incoherent beam shaping with freeform mirror*, Optical Engineering + Applications (SPIE, 2008), Vol. 7059.
62. V. Oliker, "Optical design of freeform two-mirror beam-shaping systems," *J. Opt. Soc. Am. A* **24**, 3741-3752 (2007).
63. J. Miñano, P. Benítez, J. Blen, and A. Santamaría, "Design of a novel free-form condenser overcoming rotational symmetry limitations," in *Optical Engineering + Applications*, (SPIE, 2008),
64. Y. Ding, X. Liu, Z.-r. Zheng, and P.-f. Gu, "Freeform LED lens for uniform illumination," *Opt. Express* **16**, 12958-12966 (2008).
65. S. Sorgato, R. Mohedano, J. Chaves, M. Hernández, J. Blen, D. Grabovičkić, P. Benítez, J. C. Miñano, H. Thienpont, and F. Duerr, "Compact illumination optic with three freeform surfaces for improved beam control," *Opt. Express* **25**, 29627-29641 (2017).
66. R. Wu, Z. Feng, Z. Zheng, R. Liang, P. Benítez, J. C. Miñano, and F. Duerr, "Design of Freeform Illumination Optics," *Laser & Photonics Reviews* **12**, 1700310 (2018).
67. L. W. Alvarez, "Two-element variable-power spherical lens," (1967).
68. A. W. Lohmann, "A New Class of Varifocal Lenses," *Appl. Opt.* **9**, 1669-1671 (1970).

69. L. W. Alvarez and W. E. Humphry, "Variable-power lens and system," (1970).
70. M. Bawart, A. Jesacher, S. Bernet, and M. Ritsch-Marte, "Remote focusing in confocal microscopy by means of a modified Alvarez lens," *Journal of Microscopy* **271**, 337-344 (2018).
71. A. Wilson and H. Hua, "Design and demonstration of a vari-focal optical see-through head-mounted display using freeform Alvarez lenses," *Opt. Express* **27**, 15627-15637 (2019).
72. S. S. Rege, T. S. Tkaczyk, and M. R. Descour, "Application of the Alvarez-Humphrey concept to the design of a miniaturized scanning microscope," *Opt. Express* **12**, 2574-2588 (2004).
73. J. A. Shultz and T. J. Suleski, "Design of a Variable Toric Lens Using Laterally Shifted Freeform Elements," in *Optical Design and Fabrication 2017 (Freeform, IODC, OFT)*, OSA Technical Digest (online) (Optica Publishing Group, 2017), JW2C.2.
74. S. Barbero, "The Alvarez and Lohmann refractive lenses revisited," *Opt. Express* **17**, 9376-9390 (2009).
75. P. J. Smilie and T. J. Suleski, "Variable-diameter refractive beam shaping with freeform optical surfaces," *Opt. Lett.* **36**, 4170-4172 (2011).
76. T. Suleski, J. Shultz, and P. Smilie, *Dynamic beam shaping with freeform optics*, SPIE Optical Engineering + Applications (SPIE, 2014), Vol. 9194.
77. J. Shultz, P. Smilie, B. Dutterer, M. Davies, and T. Suleski, *Experimental characterization of variable output refractive beamshapers using freeform elements*, SPIE Optical Engineering + Applications (SPIE, 2014), Vol. 9194.

78. S. Shadalou, W. J. Cassarly, and T. J. Suleski, "Tunable illumination for LED-based systems using refractive freeform arrays," *Opt. Express* **29**, 35755-35764 (2021).
79. T. J. Suleski, P. J. Smilie, and J. A. Shultz, "Dynamic laser beam shaping methods and systems," (2016).
80. I. A. Palusinski, J. M. Sasián, and J. E. Greivenkamp, "Lateral-shift variable aberration generators," *Appl. Opt.* **38**, 86-90 (1999).
81. T. Mitchell and J. Sasian, "Variable aberration correction using axially translating phase plates," in *AeroSense '99*, (SPIE, 1999),
82. E. Acosta and S. Bará, "Variable aberration generators using rotated Zernike plates," *J. Opt. Soc. Am. A* **22**, 1993-1996 (2005).
83. Cristina M. Gómez-Sarabia and J. Ojeda-Castañeda, "Tunable Optical Masks for extended Depth of Field," in *Frontiers in Optics/Laser Science*, (OSA, 2015),
84. J. Ojeda-Castañeda, C. M. Gómez-Sarabia, and S. Ledesma, "Novel free-form optical pairs for tunable focalizers," *Journal of Optics* **43**, 85-91 (2014).
85. M. Demenikov, G. Muyo, and A. R. Harvey, "Experimental demonstration of continuously variable optical encoding in a hybrid imaging system," *Opt. Lett.* **35**, 2100-2102 (2010).
86. Jorge Ojeda-Castaneda, Emmanuel Yépez-Vidal, Eloy García-Almanza, and C. M. Gómez-Sarabia, "Tunable Gaussian mask for extending the depth of field," *PHOTONICS LETTERS OF POLAND* **4**, 115-117 (2012).
87. J. Ojeda-Castañeda, E. A. Gomez, H. P. Mora, M. T. Cisneros, E. R. Ledesma Orozco, J. S. Pacheco Santamaria, J. G. Martinez Castro, and R. C. Salas Segoviano, "Optical System With Variable Field Depth," 8,159,753 B2 (2012).

88. J. Ojeda-Castañeda and C. Gómez-Sarabia, "Tunable focalizers: phase conjugate pairs," in *IV International Conference on Applications of Optics and Photonics (AOP 2019)*, (SPIE, 2019),
89. J. Ojeda-Castañeda, J. E. A. Landgrave, and C. M. Gómez-Sarabia, "Conjugate phase plate use in analysis of the frequency response of imaging systems designed for extended depth of field," *Appl. Opt.* **47**, E99-E105 (2008).
90. T. Hellmuth, A. Bich, R. Börret, A. Holschbach, and A. Kelm, "Variable phaseplates for focus invariant optical systems," in *Optical Systems Design 2005*, (SPIE, 2005),
91. L. Ledesma-Carrillo, R. Guzmán-Cabrera, C. M. Gómez-Sarabia, M. Torres-Cisneros, and J. Ojeda-Castañeda, "Tunable field depth: hyperbolic optical masks," *Appl. Opt.* **56**, A104-A114 (2017).
92. J. Ojeda-Castañeda and C. M. Gómez-Sarabia, "Tuning field depth at high resolution by pupil engineering," *Adv. Opt. Photon.* **7**, 814-880 (2015).
93. S. Shadalou and T. J. Suleski, "General design method for dynamic freeform optics with variable functionality," *Opt. Express* **30**, 19974-19989 (2022).
94. S. Moein and T. J. Suleski, "Freeform optics for variable extended depth of field imaging," *Opt. Express* **29**, 40524-40537 (2021).
95. S. Moein, S. Shadalou, and T. J. Suleski, "PSF engineering with variable logarithmic phase plates for the extended depth of field," *Opt. Continuum* **1**, 1579-1592 (2022).
96. "Edmund Optics", retrieved <https://www.edmundoptics.com/f/precision-aspheric-lenses/13139>.

97. H. Aryan, G. D. Boreman, and T. J. Suleski, "The Minimum Modulation Curve as a tool for specifying optical performance: application to surfaces with mid-spatial frequency errors," *Opt. Express* **27**, 25551-25559 (2019).
98. G. D. Boreman, *Modulation transfer function in optical and electro-optical systems*, Tutorial texts in optical engineering (SPIE), Vol. TT121.